AGU PUBLICATIONS

Tectonics

RESEARCH ARTICLE
10.1002/2015TC003948

Key Points:
- Ophiolite in the XIMAB of the CAOB formed in both ocean and subduction settings
- Ophiolite and associated magmatism reveal two cycles of accretionary events
- The XIMAB experienced soft "Appalachian-type" collision

Supporting Information:
- Tables S1–S4

Correspondence to:
S. Song,
sgsong@pku.edu.cn

Citation:
Song, S., M.-M. Wang, X. Xu, C. Wang, Y. Niu, M. B. Allen, and L. Su (2015), Ophiolites in the Xing'an-Inner Mongolia accretionary belt of the CAOB: Implications for two cycles of seafloor spreading and accretionary orogenic events, *Tectonics*, *34*, 2221–2248, doi:10.1002/2015TC003948.

Received 17 JUN 2015
Accepted 23 SEP 2015
Accepted article online 28 SEP 2015
Published online 26 OCT 2015

Ophiolites in the Xing'an-Inner Mongolia accretionary belt of the CAOB: Implications for two cycles of seafloor spreading and accretionary orogenic events

Shuguang Song[1,2], Ming-Ming Wang[1], Xin Xu[1], Chao Wang[1], Yaoling Niu[2,3], Mark B. Allen[2], and Li Su[4]

[1]MOE Key Laboratory of Orogenic Belts and Crustal Evolution, School of Earth and Space Sciences, Peking University, Beijing, China, [2]Department of Earth Sciences, University of Durham, Durham, UK, [3]Institute of Oceanology, Chinese Academy of Sciences, Qingdao, China, [4]Institute of Earth Science, Chinese University of Geosciences, Beijing, China

Abstract The Xing'an-Inner Mongolia accretionary belt in the southeastern segment of the Central Asian Orogenic Belt (CAOB) was produced by the long-lived subduction and eventual closure of the Paleo-Asian Ocean and by the convergence between the North China Craton and the Mongolian microcontinent. Two ophiolite belts have been recognized: the northern Erenhot-Hegenshan-Xi-Ujimqin ophiolite belt and the southern Solonker-Linxi ophiolite belt. Most basalts in the northern ophiolite belt exhibit characteristics of normal-type to enriched-type mid-ocean ridge basalt affinities with depleted Nd isotopic composition ($\varepsilon_{Nd}(t) > +5$), comparable to modern Eastern Pacific mid-ocean ridge basalts. Most basaltic rocks in the southern belt show clear geochemical features of suprasubduction zone-type oceanic crust, probably formed in an arc/back-arc environment. The inferred back-arc extension along the Solonker-Linxi belt started at circa 280 Ma. Statistics of all the available age data for the ophiolites indicates two cycles of seafloor spreading/subduction, which gave rise to two main epochs of magmatic activity at 500–410 Ma and 360–220 Ma, respectively, with a gap of ~50 million years (Myr). The spatial and temporal distribution of the ophiolites and concurrent igneous rocks favor bilateral subduction toward the two continental margins in the convergence history, with final collision at ~230–220 Ma. In the whole belt, signals of continental collision and Himalayan-style mountain building are lacking. We thus conclude that the Xing'an-Inner Mongolia segment of the CAOB experienced two cycles of seafloor subduction, back-arc extension, and final "Appalachian-type" soft collision.

1. Introduction

The Central Asian Orogenic Belt (CAOB) is generally thought to have resulted from the closure of the Paleo-Asian Ocean, which lay between the two major continents of the North China Craton (NCC) and the Siberian Craton [e.g., *Jahn et al.*, 2000; *Jahn*, 2004; *Buslov et al.*, 2001; *Badarch et al.*, 2002; *Windley et al.*, 1990, 2007; *Xiao et al.*, 2003, 2009a, 2009b, 2013; *Cocks and Torsvik*, 2007; *Kröner et al.*, 2007]. However, it remains debatable as to when the Paleo-Asian Ocean started and finally closed and where the ultimate suture is located [e.g., *Chen et al.*, 2000; *Li*, 2006; *Xiao et al.*, 2009a; *Han et al.*, 2011; *Xu et al.*, 2013; *Eizenhöfer et al.*, 2014]. It is also unclear whether this huge orogenic belt had been a long-lived, incessant, and independent event or it had evolved with discontinuous, multiple stages or cycles of orogenic movements during its long histories. Meanwhile, many researchers declared that this huge orogenic belt is an accretionary orogenic belt that had evolved for a long period of time since the Neoproterozoic [e.g., *Kröner et al.*, 2007; *Windley et al.*, 2007; *Xiao et al.*, 2009a; *Long et al.*, 2012], rather than a collisional orogen like the Himalaya. Others suggested that it had an orogenic process of strong collision, mountain building, long period of postcollisional delamination, extension, and relevant magmatism [*Jahn et al.*, 2009; *Han et al.*, 2011; *Xu et al.*, 2013]. Several subdivision schemes in terms of the tectonic architecture, e.g., multiple suture zones, multiple accretion complexes, and multiple orogenic belts, of the eastern part of the CAOB have been proposed [*Wang and Liu*, 1986; *Chen et al.*, 2000; *Badarch et al.*, 2002; *Xiao et al.*, 2003, 2009a; *Xu et al.*, 2013, 2014; *Eizenhöfer et al.*, 2014], which made this region more confusing to understand.

Ophiolites, as fragments of ancient oceanic lithosphere [e.g., *Coleman*, 1977; *Dewey and Bird*, 1971], play irreplaceable roles in the recognition and reconstruction of the evolution history of an ancient ocean, including the opening, closure, development of subduction system(s), and the consequent orogeny [*Dilek*, 2003; *Dilek et al.*, 2007; *Dilek and Furnes*, 2011; *Song et al.*, 2013]. Ophiolites occur in both collisional-type

(i.e., Alpine, Himalayan, and Appalachian) and accretionary-type (i.e., North American Cordilleran) orogenic belts, marking major fossil plate boundaries between amalgamated plates or accreted terranes [*Lister and Forster*, 2009; *Dilek and Furnes*, 2011]. Two essential types, the subduction-unrelated ophiolites and subduction-related ophiolites, were summarized by *Dilek and Furnes* [2011]. The subduction-unrelated ophiolites include continental margin, mid-ocean ridge with normal and enriched MORB signatures, and plume type (plume proximal ridge and oceanic plateau). Subduction-related ophiolites include suprasubduction zone and volcanic arc types (also known as suprasubduction zone type (SSZ type)).

The Xing'an-Inner Mongolia accretionary belt of the CAOB, with an area of 1,600,000 km^2, is a ~400 km wide and highly debated orogenic belt that has been extensively studied for more than 20 years. This belt is characterized by various accretionary complexes, interpreted as island arcs, fore-arc or back-arc basins, ophiolites, and microcontinents, dating from the Neoproterozoic to the Mesozoic [e.g., *Xiao et al*., 2003, 2009a; *Xu et al*., 2013]. It is also distinguished by the massive generation of juvenile crust in the Phanerozoic [*Jahn et al*., 2000; *Jahn*, 2004; *Kröner et al*., 2007; *Windley et al*., 2007]. Ophiolites in this belt have drawn particular attention to their petrography, geochemistry, and geochronology [*Liu et al*., 2003; *Miao et al*., 2007, 2008; *Xiao et al*., 2003, 2009a; *Jian et al*., 2008, 2010, 2012; *Liu et al*., 2013; *Z. Zhang et al*., 2015]. Plutonic and volcanic rocks along this orogenic belt have also been extensively documented in the last two decades [see *Xu et al*., 2014].

Though extensively studied, high-precision geochemical and age data for these ophiolites or suspected ophiolite suites are limited. In this paper, we present new data for ophiolites in the Linxi-Xi-Ujimqin region. We also provide a comprehensive summary for ophiolites and the concurrent igneous rocks and their spatio-temporal constraints that allow the reconstruction of the evolution history of the Xing'an-Inner Mongolia accretionary belt.

2. Geological Setting

The Xing'an-Inner Mongolia accretionary belt of the CAOB extends in the ENE direction for more than 2000 km between the NCC and the South Mongolia microcontinent. It is bordered by the Chifeng-Bayan Oba Fault, or by the Xar Moron Fault, to the south and by the Chagan Obo-Arongqi Fault to the north [*Xiao et al*., 2003]. The width of this belt exceeds 400 km (Figure 1).

Division and nomenclature of the tectonic units in this accretionary belt is quite confused. Several tectonic belts/units, including various suture zones, arcs, orogenic belts, and microcontinent blocks, have been divided by different authors with different approaches [e.g., *Xiao et al*., 2003, 2009a; *Miao et al*., 2007, 2008; *Jian et al*., 2008, 2012; *Xu et al*., 2013, 2014].

As shown in Figure 1, volcanic rocks of Paleozoic age are widespread in the whole accretionary belt, as well as the two continental margins of the NCC and the Mongolia microcontinent. Granitoid plutons, on the other hand, are mainly distributed in three belts, the southern margin of the Mongolia microcontinent, the center of the Xing'an-Inner Mongolia accretionary belt (XIMAB), and the northern margin of the NCC. Both sides of the Xing'an-Inner Mongolia accretionary belt can be considered as Andean-type active continental margins on the basis of their intensive, contemporaneous magmatic activities with ages from Early Paleozoic to Early Triassic [e.g., *Xiao et al*., 2003, 2009a; *Xu et al*., 2014; *S. Zhang et al*., 2014]. Therefore, the studied Xing'an-Inner Mongolia accretionary belt should be the product of convergence between the NCC and the Mongolian microcontinent.

The Xing'an-Inner Mongolia accretionary belt of the CAOB mainly consists of ophiolite blocks/fragments, Paleozoic to Mesozoic volcanic-sedimentary sequences and sedimentary strata, and igneous plutons of varying composition and age from the Early Paleozoic to Mesozoic. In fact, the overall number of recognized ophiolite suites or suspected ophiolite complexes is relatively small: fewer than 20; they are sparsely scattered in the vast zone of the Xing'an-Inner Mongolia segment of the CAOB. We agree that two ophiolite belts can be roughly subdivided [e.g., *Xiao et al*., 2003; *Miao et al*., 2007; *Jian et al*., 2010; *J. Zhang et al*., 2015]: the Solonker-Linxi SSZ-type ophiolite belt in the south and the Erenhot-Hegenshan-Xi-Ujimqin ophiolite belt in the north. These two belts are separated by the Baolidao-Xilinhot metamorphic-volcanic complex (or arc complex) (Figure 1). Of the ophiolite blocks/fragments, only two (gabbros from Tulinkai and Sunidzouqi; see Figure 1 for localities) have been determined to form in the Early Paleozoic [*Liu et al*., 2003; *Jian et al*., 2008].

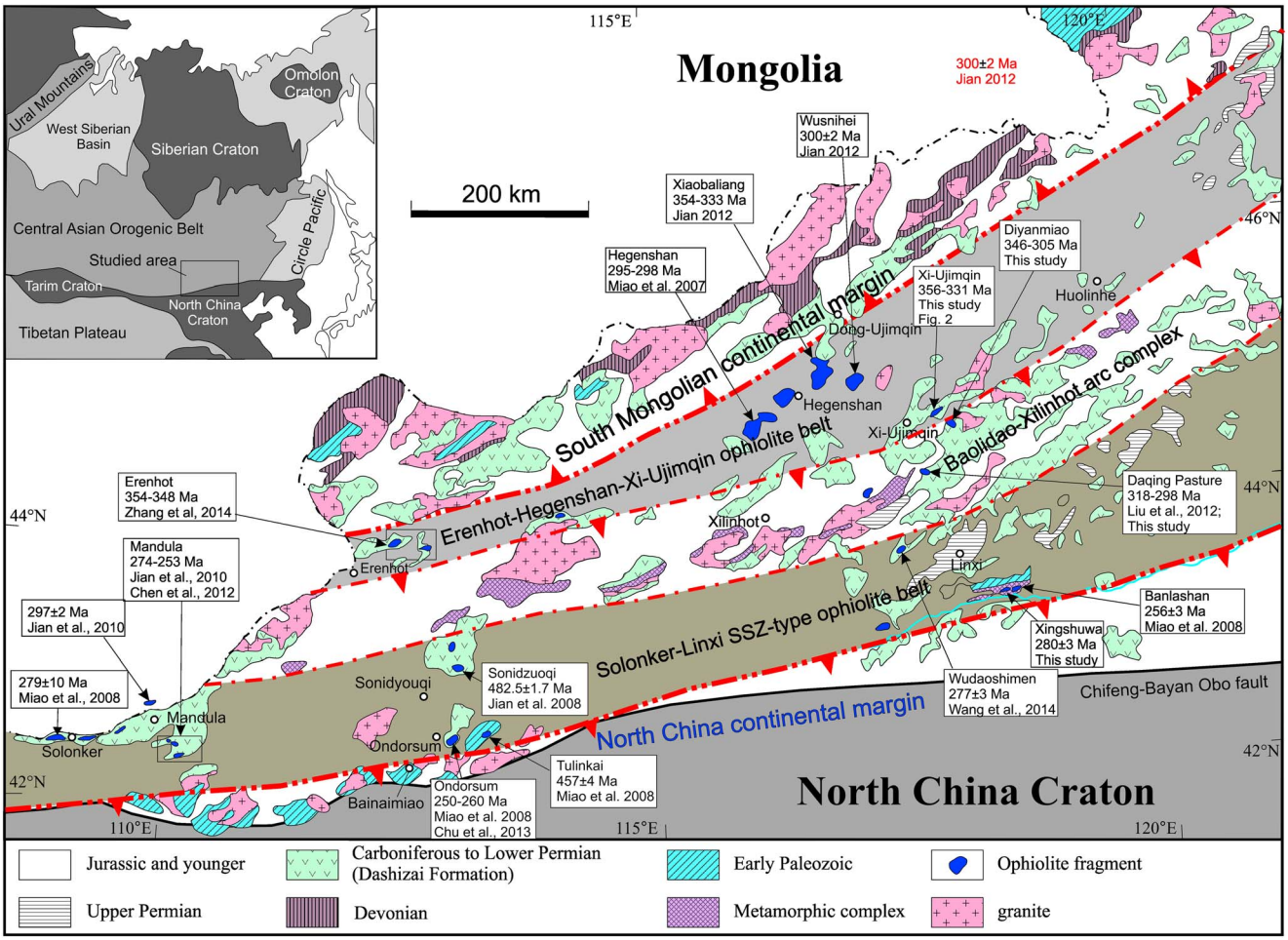

Figure 1. Geological map of the Xing'an-Inner Mongolia Accretionary Belt of the CAOB showing tectonic units (modified after *Xiao et al.* [2003] and *Miao et al.* [2007]).

Volcanic-sedimentary sequences in the XIMAB include (1) the Early Paleozoic Bainaimiao Group and (2) the Late Paleozoic Dashizhai Formation. The Bainaimiao volcanic-sedimentary sequence is located in the western part of the Xing'an-Inner Mongolia segment, the boundary line between the NCC and the CAOB, and consists of arc-type volcanic rocks of pre-Devonian (>420 Ma) age [*Bureau of Geology and Mineral Resources of Inner Mongolia* (*BGMRIM*), 1991; *Hsü et al.*, 1991; *Xiao et al.*, 2003; *Jian et al.*, 2008; *Li et al.*, 2015]. *Xiao et al.* [2003] suggested that a south dipping subduction zone near the present position of the Ondorsum mélange in the Ordovician gave rise to the Bainaimiao arc. The Dashizhai volcanic sequence is widespread in the whole area of the Xing'an-Inner Mongolia segment, occurring interlayered with Carboniferous and Permian sedimentary strata with ages ranging from 315 to 250 Ma (see below). Contemporaneous volcanic rocks also occur in the two continental margins of the NCC and the South Mongolia block [*BGMRIM*, 1991].

Metamorphic rocks occur discontinuously along a NEE direction in a belt in the middle section of the XIMAB. They have been named the "Xilinguole complex" and considered to be Precambrian basement with some rocks of Mesoproterozoic age [*BGMRIM*, 1991; *Xu et al.*, 2013]. This metamorphic complex mainly consists of greenschist facies to upper amphibolite facies metamorphosed sedimentary and volcanic rocks, but its metamorphic age is poorly constrained. Together with the well-developed igneous rocks, a metamorphic-magmatic belt was determined by *Xiao et al.* [2003, 2009a], namely, "the Baolidao island arc," as a consequence of northward seafloor subduction.

Therefore, a significantly improved understanding of the tectonic evolution of the orogenic belt is now emerging thanks to detailed studies on ophiolites and relevant igneous rocks, which enable us to make a new and simplified subdivision for tectonic units from north to south: the South Mongolian active continental margins

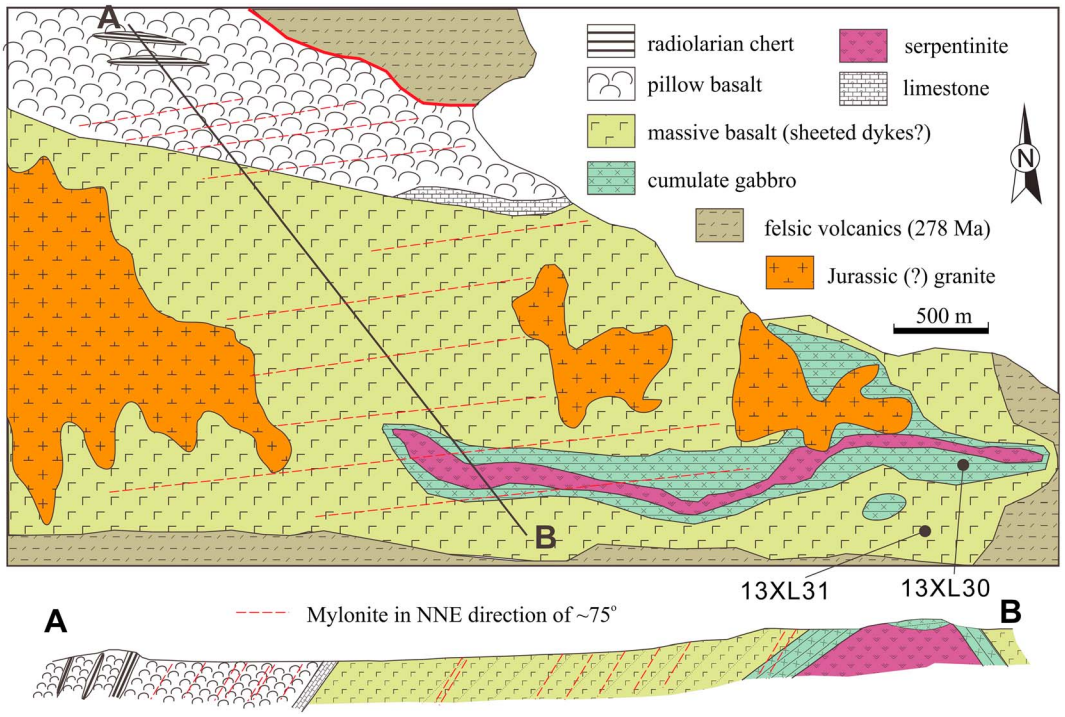

Figure 2. Geological map of the Xi-Ujimqin ophiolite with dated gabbro and sheeted dyke (?) samples (revised after *Li et al*. [2012]).

along the southern part of the Mongolian microcontinent, the Erenhot-Hegenshan-Xi-Ujimqin ophiolitic accretionary belt, the Baoligdao-Xilinhot arc complex, the Solonker-Linxi back-arc belt with SSZ-type ophiolites, and the North China continental margin along the northern NCC (Figure 1).

3. Analytical Methods

3.1. Bulk Rock Major and Trace Elements Analyses

Bulk rock major and trace elements analysis was done at the Geological Lab Center, China University of Geosciences, Beijing (CUGB). Major elements were analyzed using a Leeman Prodigy inductively coupled plasma-optical emission spectroscopy system with high-dispersion Echelle optics. Based on rock standards AGV-2, W-2 (U.S. Geological Survey: USGS), GRS-1, and GSR-3 (national geological standard reference material of China), the analytical precisions (1σ) for most major elements are better than 1% with the exception of TiO_2 (~1.5%) and P_2O_5 (~2.0%). Loss on ignition was determined by placing 1 g of samples in the furnace at 1000°C for several hours before being cooled in a desiccator and reweighed.

Bulk rock trace element analysis was done on an Agilent-7500a inductively coupled plasma-mass spectrometry (ICP-MS) at the Institute of Earth Science, China University of Geosciences, Beijing. Roughly 40 mg of sample powder was dissolved in an equal mixture of subboiling distilled HNO_3 and HF with a Teflon digesting vessel on a hot plate at 285°C for 48 h using high-pressure bombs to aid digestion/dissolution. The sample was then evaporated to incipient dryness, refluxed with 6 N HNO_3, and heated again to incipient dryness. The sample was then dissolved in 2 mL of 3 N HNO_3 using high-pressure bombs for a further 24 h to ensure complete digestion/dissolution. After digestion, the sample was diluted with Milli-Q water (18 MΩ) to a final dilution factor of 2000. Rock standards AGV-2, W-2, and BHVO-2 (USGS) were used to monitor the analytical accuracy and precision. Analytical accuracy, as indicated by relative difference between measured and recommended values, is better than 5% for most elements and 10–15% for Cu, Zn, Gd, and Ta.

3.2. In Situ Zircon U-Pb Dating

Six samples including gabbro, sheeted dyke, and pillow basalt were chosen for in situ zircon U-Pb dating. Zircon grains were separated by standard heavy-liquid and magnetic techniques and purified by

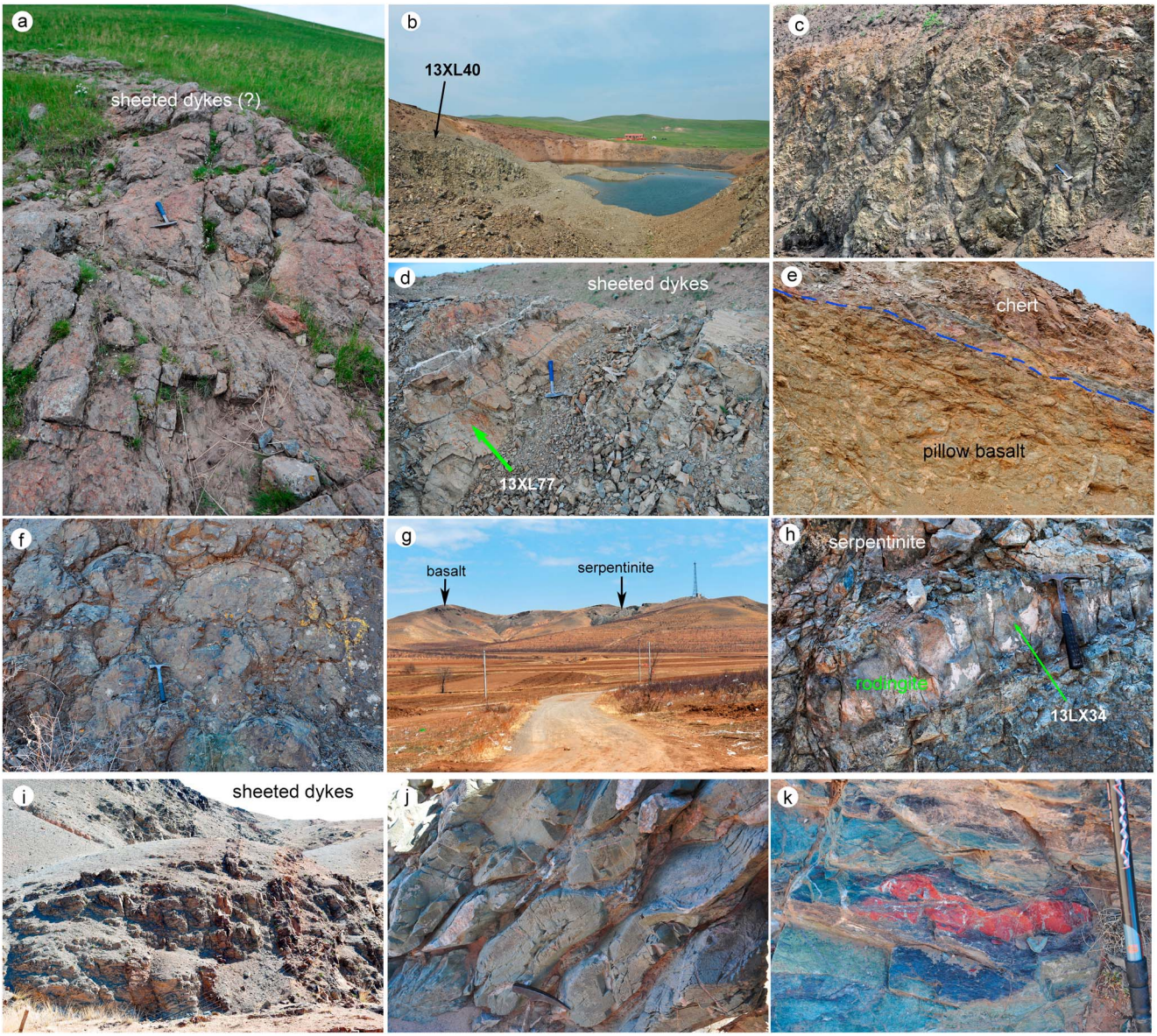

Figure 3. Photos showing various lithologies of ophiolites in the XIMAB. (a) Massive basalts (sheeted dyke?) in the Xi-Ujimqin ophiolite; single-chilled margins cannot be seen due to the weathering. (b and c) Spilitic basalt with pillow structure in the Diyanmiao ophiolite. (d) Sheeted dykes with 100% diabase dykes and ambiguous single-sided chilling border in the Daqing pasture ophiolite. (e) Pillow basalts and red chert that strongly deformed by late thrusting fault in the Daqing pasture ophiolite. (f) Pillow basalts in the Wudaoshimen region. (g) Far view of the Xingshuwa ophiolite. (h) Rodingite dyke in serpentinite in the Xingshuwa ophiolite. (i) Sheeted dykes in the Ondorsum ophiolite. (j) Deformed pillow basalts in the Ondorsum ophiolite. (k) Red radiolarian chert in the Ondorsum ophiolite.

handpicking under a binocular microscope at the Langfang Regional Geological Survey, China. They were then embedded in epoxy resin discs and polished down to about half-sections to expose the grain interiors. Cathodoluminescence (CL) images were acquired to observe the internal structures of zircon grains, using a CL spectrometer (Garton Mono CL3+) equipped on a Quanta 200F environmental scanning electron microscope at scanning conditions of 15 kV and 120 nA at Peking University.

Measurement of U-Th-Pb isotopes for samples 13XL30, 13XL31, 13XL40, 13XL59, and 13XL77 was done using a Cameca IMS-1280 SIMS in the Institute of Geology and Geophysics, Chinese Academy of Sciences in Beijing. The instrument description and analytical procedure are given in *Li et al.* [2009]. The primary O_2^- ion beam spot is about 20–30 μm in size. Analysis of the standard zircon Plésovice was interspersed with analysis of unknowns. Each measurement consists of seven cycles. Pb/U calibration was performed relative to zircon

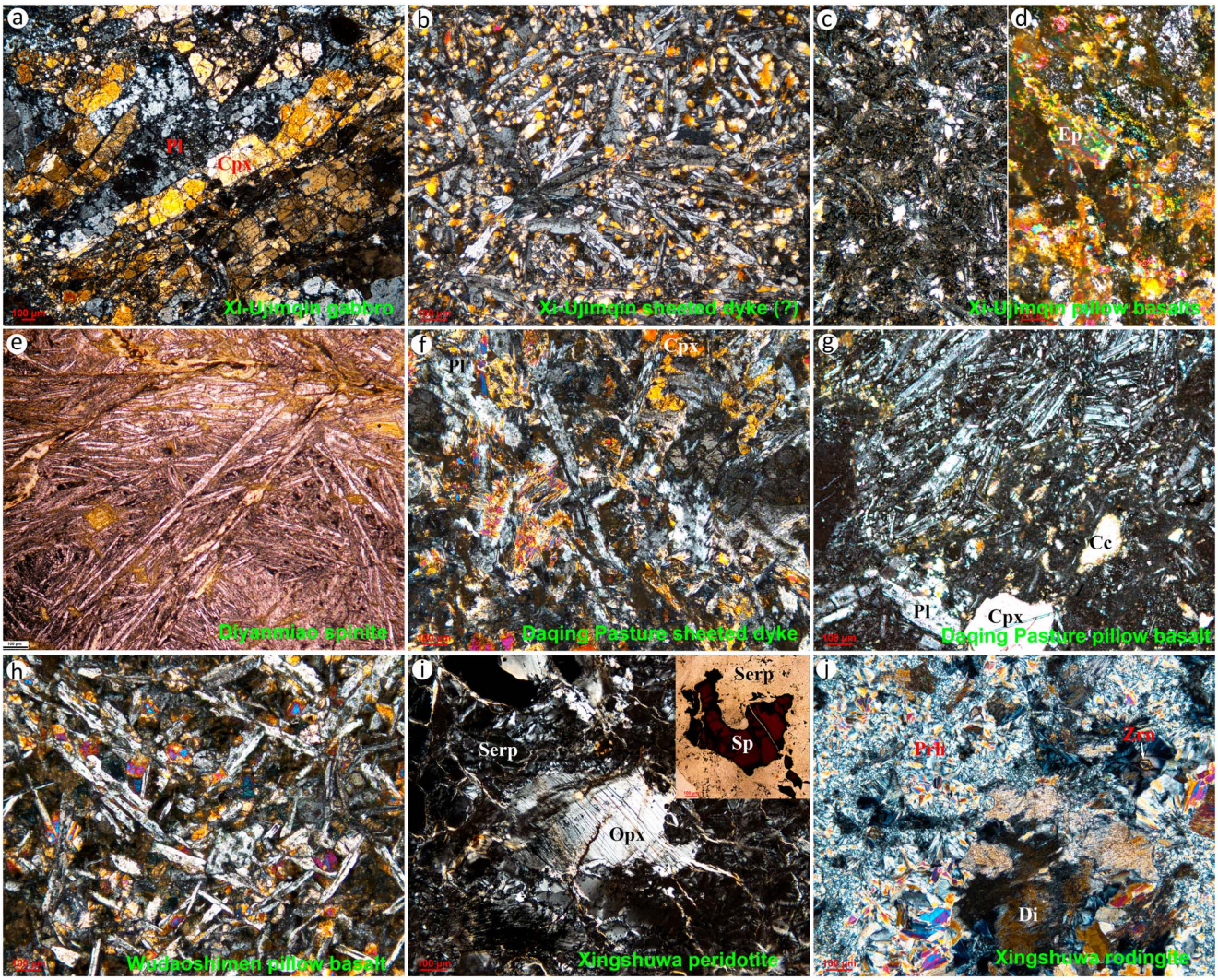

Figure 4. Photomicrographs of various rocks in ophiolites from the XIMAB. (a) Mylonitized gabbro showing elongated clinopyroxenes (Cpx) and dynamic recrystallized plagioclase (13XL30, Xi-Ujimqin ophiolite). (b) Ophitic (or intergranular) texture of the massive basalt (sheeted dyke?) showing well-developed plagioclase laths with fine-grained Cpx (13XL31, Xi-Ujimqin ophiolite). (c) Weakly altered pillow basalts with pilotaxitic texture (13XL-34, Xi-Ujimqin ophiolite). (d) Strongly altered pillow basalts with epidote (Ep) (13XL-35, Xi-Ujimqin ophiolite). (e) Pillow basalt showing spilite texture with long, skeletal or acicular intergrown crystals of albite + clinopyroxene (13XL40, Diyanmiao ophiolite). (f) Ophitic texture of the sheeted dyke (13XL-77, Daqing pasture ophiolite). (g) Pilotaxitic texture of the pillow basalt with Cpx phenocryst (13XL-63, Daqing pasture ophiolite). (h) Ophitic texture of the pillow basalt (13LX-02, Wudaoshimen). (i) Serpentized harzburgite with deformed orthopyroxene (Opx) and spinel (Sp) (right corner) (13LX38, Xingshuwa ophiolite). (j) Rodingite showing diopside (Di) and prehnite (Prh) with a fine-grained zircon (Zrn). Grossular is not shown in this photo (13LX34, Xingshuwa ophiolite).

standard Plésovice (337 Ma) [*Sláma et al*., 2008]; U and Th concentrations were calibrated against zircon standard 91500 [*Wiedenbeck et al*., 1995]. A long-term uncertainty of 1.5% (1σ relative standard deviation, RSD) for $^{206}Pb/^{238}U$ measurements of the standard zircons was propagated to the unknowns [*Li et al*., 2010], despite that the measured $^{206}Pb/^{238}U$ error in a specific session is generally 1% (1σ RSD). Measured compositions were corrected for common Pb using nonradiogenic ^{204}Pb. Corrections are sufficiently small to be insensitive to the choice of common Pb composition, and an average of present-day crustal composition [*Stacey and Kramers*, 1975] is used for the common Pb assuming that the common Pb is largely a surface contamination introduced during sample preparation. Data reduction was carried out using the Isoplot/Ex v. 3.0 program [*Ludwig*, 2003]. Uncertainties on individual analyses in data tables are reported at 1σ level; Concordia U-Pb ages are quoted with 95% confidence level. In order to monitor the external uncertainties of SIMS U-Pb zircon dating calibrated against Plésovice standard, an in-house zircon standard Qinghu was alternately analyzed as an unknown together with other unknown zircons. The measurements on Qinghu zircon yield Concordia

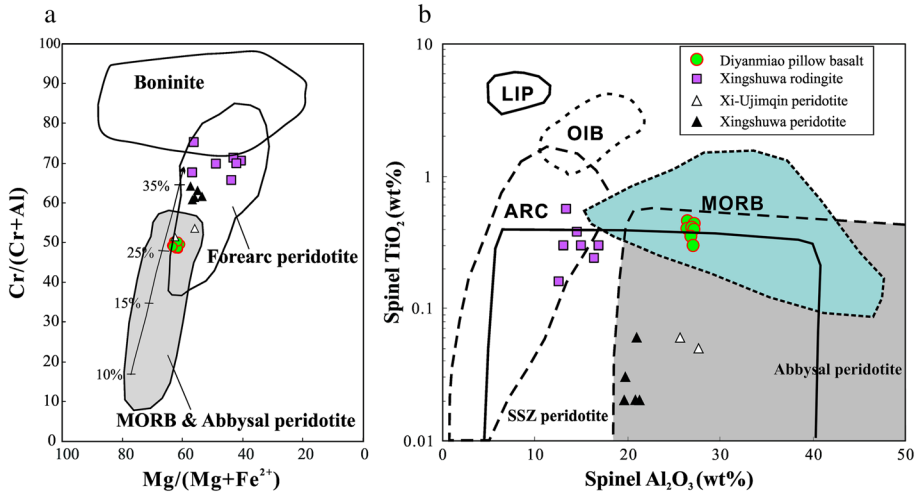

Figure 5. (a) Cr# [Cr/(Cr + Al)] versus Mg# [Mg/(Mg + Fe^{2+})] diagram for spinels from Diyanmiao pillow basalts, Xingshuwa rodingites, and peridotites of ophiolites in the XIMAB. Ranges of the MORB and abyssal peridotite are from *Dick and Bullen* [1984] and *Tamura and Arai* [2006], and range of boninite is from *Xia et al.* [2012]. Melting trend (annotated by % melting) is from *Pearce et al.* [2000]. (b) TiO_2 versus Al_2O_3 diagram for spinels in rocks of ophiolites in the XIMAB [after *Kamenetsky et al.*, 2001].

ages of 160.2 ± 0.8 Ma and 159.3 ± 1.9 Ma, which are identical within error with the recommended value of 159.5 ± 0.2 Ma [*Li et al.*, 2013].

Measurements of U-Th-Pb isotopes for sample 13LX34 were carried out on an Agilent-7500a quadrupole inductively coupled plasma-mass spectrometry coupled with a New Wave SS UP193 laser sampler (LA-ICP-MS) at CUGB. Laser spot size of 36 μm, laser energy density of 8.5 J/cm^2, and a repetition rate of 10 Hz were applied for analysis. National Institute of Standards and Technology 610 glass and Harvard zircon 91500 [*Wiedenbeck et al.*, 1995] were used as external standards, Si as internal standard, and zircon standard TEMORA (417 Ma) from Australia [*Black et al.*, 2003] as the secondary standard. The software GLITTER (ver. 4.4, Macquarie University) was used to process the isotopic ratios and element concentrations of zircons. The common lead correction was done following *Andersen* [2002]. Age calculations and plots of concordia diagrams were made using Isoplot/Ex v. 3.0 program [*Ludwig*, 2003]. Analytical details are described in *Song et al.* [2010].

All the results for zircon U-Pb analyses are given in Tables S1 and S2 in the supporting information.

3.3. Bulk Rock Sr-Nd Isotope Analyses

Separation and purification of Rb, Sr, Sm, and Nd were done using conventional ion exchange procedures in the ultraclean room of MOE key laboratory of orogenic belts and crustal evolution, Peking University. The Sr and Nd isotopic ratios were measured using a Thermo-Finnigan Triton thermal ionization mass spectrometer at Tianjin Institute of Geology and Mineral Resources. The $^{87}Rb/^{86}Sr$ and $^{147}Sm/^{144}Nd$ ratios were calculated based on Rb, Sr, Sm, and Nd contents determined by ICP-MS. Mass fractionation was corrected by normalizing the measured $^{87}Sr/^{86}Sr$ and $^{143}Nd/^{144}Nd$ against $^{86}Sr/^{88}Sr$ ratio of 0.1194 and $^{146}Nd/^{144}Nd$ ratio of 0.7219, respectively. Rock standard BCR-2 was used to evaluate the separation and purification process of Rb, Sr, Sm, and Nd, which yielded weighted mean $^{87}Sr/^{86}Sr$ ratio of 0.704992 ± 7 (2σ, n = 94) and $^{143}Nd/^{144}Nd$ ratio of 0.512634 ± 1 (2σ, n = 97). In order to monitor the data quality during the course of analysis, National Bureau of Standards 987 Sr standard and LRIG Nd standard were analyzed and gave weighted mean $^{87}Sr/^{86}Sr$ ratio of 0.710240 ± 2 (2σ, n = 96) and $^{143}Nd/^{144}Nd$ ratio of 0.512198 ± 3 (2σ, n = 46).

4. Results

4.1. The Xi-Ujimqin Ophiolite

The Xi-Ujimqin ophiolite is located at 44°29′42″N, 118°8′2″E, ~43 km east of Xi-Ujimqin county town (Figure 1), and was first reported by *Li et al.* [2012]. The outcrops are of poor quality, and contacts between various rock types in this ophiolite complex are not well exposed in the field. The lithologies include strongly serpentinized

Table 1a. Whole-Rock Major and Trace Element Compositions of Xi-Ujimqi Ophiolite in the XIMAB[a]

	Xi-Ujimqi Ophiolite							
	13XL-28	13XL-29	13XL-30	13XL-31a	13XL-31b	13XL-32	13XL-33	13XL-34
Sample	SD	SD	Gabbro	SD	SD	Gabbro	PB	PB
SiO_2	48.40	47.79	48.45	47.99	46.39	45.54	50.55	49.07
TiO_2	1.33	1.20	0.17	0.80	0.93	1.17	1.17	1.33
Al_2O_3	17.06	17.09	15.08	19.03	18.32	12.68	13.30	13.40
Fe_2O_3t	9.68	9.19	4.86	7.04	7.18	9.71	11.06	10.57
MnO	0.16	0.16	0.09	0.10	0.10	0.26	0.16	0.17
MgO	7.97	7.78	11.71	6.93	7.52	8.49	7.04	7.51
CaO	11.25	12.87	17.32	13.16	13.48	17.51	9.01	9.66
Na_2O	2.67	2.67	0.29	3.18	3.30	0.21	3.14	3.75
K_2O	0.82	0.54	0.16	0.20	0.20	0.03	0.15	0.16
P_2O_5	0.15	0.14	0.01	0.06	0.07	0.14	0.10	0.11
LOI	0.80	0.73	1.00	1.64	1.64	4.42	3.35	3.35
Mg#	65.8	66.4	84.9	69.7	70.9	67.1	59.8	62.3
				Trace Elements (ppm)				
Li			19.51		31.96			23.5
Sc	21.66	20.46	56.76	24.100	66.84	8.830	31.760	78.04
Ti	8569	7512	1019	5336	5555	7866	9196	7959
V	230.6	213.8	190.8	213.4	346.4	291.5	343.0	490.8
Cr	309.6	303.2	1621.2	293.2	477.0	17.4	242.6	348.0
Co	37.46	34.82	38.02	29.60	44.06	26.89	43.74	56.76
Ni	128.61	142.52	247.20	101.36	146.22	26.87	69.22	87.86
Cu	18.41	40.16	53.06	5.29	7.04	7.92	72.66	84.3
Zn	73.87	60.30	21.86	29.12	34.60	61.10	73.32	76.02
Ga	16.29	14.93	9.89	12.71	14.50	14.88	13.31	14.056
Rb	19.75	16.17	4.47	3.23	5.00	0.47	3.89	4.944
Sr	192.4	192.5	91.2	243.2	277.4	408.0	208.6	208.6
Y	26.00	23.38	6.47	20.04	24.80	18.03	31.98	34.5
Zr	55.51	45.56	5.01	43.36	45.98	56.83	83.84	78.047
Nb	2.417	2.332	0.166	1.044	1.045	1.963	1.397	1.368
Cs	2.181	3.474	0.087	0.071	0.184	0.035	0.579	1.246
Ba	82.02	49.86	34.20	68.80	61.28	16.52	58.30	46.88
La	3.923	3.626	0.312	1.781	1.832	3.744	2.532	2.296
Ce	12.363	10.876	0.569	5.842	5.892	11.168	8.900	7.902
Pr	2.053	1.846	0.138	1.064	1.057	1.785	1.614	1.423
Nd	10.350	9.330	0.861	5.922	6.086	8.628	8.750	8.064
Sm	3.407	3.062	0.380	2.278	2.336	2.663	3.298	2.980
Eu	1.228	1.143	0.170	0.784	0.757	2.072	1.228	1.083
Gd	4.494	4.004	0.638	3.282	3.188	3.409	4.784	4.090
Tb	0.807	0.720	0.121	0.604	0.561	0.607	0.908	0.747
Dy	5.128	4.550	0.898	3.928	3.726	3.871	6.046	5.062
Ho	1.113	0.995	0.208	0.868	0.780	0.852	1.356	1.094
Er	3.062	2.742	0.635	2.408	2.218	2.393	3.850	3.190
Tm	0.439	0.392	0.092	0.341	0.313	0.349	0.575	0.464
Yb	2.651	2.374	0.604	2.072	1.918	2.181	3.624	2.958
Lu	0.378	0.344	0.091	0.301	0.277	0.323	0.547	0.440
Hf	1.517	1.331	0.140	1.177	1.198	1.557	2.115	2.096
Ta	0.228	0.180	0.015	0.118	0.066	0.126	0.095	0.085
Pb	13.654	3.354	0.273	0.708	0.509	2.413	0.731	0.638
Th	0.394	0.262	0.006	0.074	0.030	0.158	0.124	0.070
U	0.137	0.098	0.006	0.034	0.024	0.141	0.055	0.032

[a]SD = sheeted dyke; PB = pillow basalt.

peridotite (mantle section), cumulate gabbro, pillow and massive basalts, and radiolarian chert (Figure 2). The serpentinite occurs within the cumulate gabbro and is strongly foliated. No ultramafic cumulate has been found in this section. Some massive basalts show ambiguous structure of sheeted dykes (Figure 3a), which may reflect the spreading center. The pillow basalts occur as a layer of ~500 m in thickness.

Table 1b. Whole-Rock Major and Trace Element Compositions of Diyanmiao Ophiolite in the XIMAB

	Diyanmiao Ophiolite											
	13XL-40	13XL-41	13XL-48	13XL-50	13XL-55	13XL-57	13XL-58	13XL-59	13XL-61	13XL-42	13XL-43	13XL-44
Sample	PB	PB	PB	PB	PB	PB	PB	Gabbro	Gabbro	PB	PB	PB
SiO_2	50.89	53.65	51.89	47.99	51.84	50.19	42.01	44.46	45.46	46.31	50.25	45.22
TiO_2	0.825	0.825	0.838	0.873	1.449	0.816	0.844	0.095	0.374	0.812	0.746	0.718
Al_2O_3	12.53	11.07	12.74	13.45	13.13	12.83	13.07	15.55	10.46	12.30	11.58	10.47
Fe_2O_3t	8.85	7.90	8.64	9.76	10.00	8.86	10.42	3.56	8.35	9.08	8.83	8.83
MnO	0.172	0.139	0.151	0.167	0.184	0.151	0.234	0.075	0.315	0.195	0.145	0.220
MgO	8.97	8.59	8.47	10.14	7.48	9.65	5.15	9.81	13.85	6.46	4.76	5.02
CaO	10.48	10.14	9.60	10.18	8.34	9.89	16.28	21.67	17.30	17.12	15.89	21.27
Na_2O	3.90	3.40	4.00	3.28	4.13	3.64	1.94	0.17	0.37	2.56	2.21	1.64
K_2O	0.09	0.07	0.11	0.14	0.11	0.07	0.77	0.02	0.02	0.46	0.04	0.06
P_2O_5	0.063	0.069	0.063	0.069	0.423	0.067	0.082	0.017	0.024	0.073	0.081	0.062
LOI	3.01	3.99	3.35	3.76	2.73	3.68	9.04	4.44	3.32	4.49	5.30	6.28
Mg#	70.3	71.7	69.5	70.8	44.8	71.7	53.5	86.5	79.4	62.4	55.7	57.0
	Trace Elements (ppm)											
Li	18.30	19.36	17.33	27.97	15.14	22.56	15.73	8.95	10.19	9.85	7.52	8.74
Sc	34.84	34.08	36.43	38.54	21.99	35.06	29.58	17.22	37.07	31.34	29.98	20.41
Ti	4945	4945	5023	5232	8686	4889	5062	571	2241	4869	4472	4305
V	226.9	197.1	233.8	241.9	176.5	221.3	233.6	75.1	220.5	242.9	251.1	226.7
Cr	449.4	457.1	485.9	509.5	13.2	445.4	28.9	464.1	504.6	410.7	397.6	344.7
Co	39.06	36.63	41.94	44.99	16.29	40.81	26.21	20.80	37.80	31.90	37.70	32.09
Ni	154.73	174.38	197.24	184.42	14.95	173.34	15.38	125.14	160.66	109.12	127.89	97.45
Cu	72.56	56.77	87.82	71.91	31.40	74.31	52.99	32.00	35.52	57.22	50.15	72.45
Zn	60.98	55.38	59.66	72.71	119.40	60.45	79.00	20.01	42.50	55.58	72.09	49.18
Ga	10.02	9.14	9.89	12.19	21.67	11.07	15.53	10.34	10.52	14.17	14.93	14.15
Rb	1.35	0.95	1.70	2.73	2.19	1.00	14.62	0.32	0.20	5.15	0.60	0.66
Sr	156.4	107.8	155.1	164.0	688.8	125.5	319.8	56.2	66.5	164.6	92.1	106.8
Y	16.07	15.78	16.33	18.12	31.60	16.00	14.50	3.31	10.20	16.56	17.51	13.63
Zr	56.59	55.43	57.03	59.49	156.78	54.77	34.15	24.04	9.74	51.99	49.69	44.49
Nb	0.66	0.63	0.67	0.68	2.56	0.63	0.46	0.17	0.13	0.61	0.59	0.51
Cs	0.81	0.85	1.17	1.29	0.47	1.09	0.86	0.05	0.07	0.58	0.85	0.39
Ba	28.30	29.45	35.54	40.07	28.02	38.12	89.24	4.08	10.87	135.22	29.34	35.91
La	1.69	1.35	1.55	1.83	6.14	1.81	2.47	0.96	0.27	1.85	2.11	1.63
Ce	5.83	4.97	5.54	6.42	18.83	6.03	6.81	2.04	1.04	5.97	5.51	5.00
Pr	1.01	0.90	0.96	1.10	3.01	1.01	1.09	0.27	0.21	1.02	1.04	0.87
Nd	5.37	4.90	5.29	5.96	15.17	5.38	5.54	1.07	1.31	5.35	5.54	4.54
Sm	1.79	1.73	1.79	1.97	4.43	1.76	1.76	0.28	0.61	1.75	1.79	1.49
Eu	0.77	0.70	0.75	0.81	1.77	0.79	0.74	0.14	0.29	0.86	0.80	0.73
Gd	2.44	2.38	2.53	2.75	5.63	2.44	2.31	0.41	1.11	2.53	2.50	2.13
Tb	0.47	0.45	0.47	0.51	0.95	0.47	0.40	0.09	0.24	0.45	0.47	0.39
Dy	2.96	2.90	3.00	3.32	5.77	2.92	2.51	0.53	1.68	2.94	3.02	2.49
Ho	0.66	0.66	0.68	0.75	1.25	0.65	0.57	0.14	0.41	0.65	0.69	0.57
Er	2.01	2.00	1.99	2.16	3.68	1.94	1.69	0.41	1.29	1.96	2.04	1.71
Tm	0.28	0.27	0.28	0.30	0.50	0.27	0.24	0.07	0.19	0.27	0.28	0.24
Yb	1.79	1.78	1.80	1.98	3.22	1.75	1.54	0.43	1.28	1.75	1.82	1.53
Lu	0.28	0.27	0.28	0.31	0.50	0.27	0.25	0.08	0.20	0.27	0.29	0.24
Hf	1.59	1.52	1.56	1.66	3.89	1.48	1.13	0.54	0.39	1.44	1.37	1.24
Ta	0.08	0.05	0.06	0.05	0.16	0.06	0.02	0.14	0.02	0.05	0.04	0.02
Pb	0.38	0.74	0.41	0.28	2.82	1.18	1.80	3.41	0.61	3.41	1.18	1.08
Th	0.12	0.04	0.08	0.06	0.42	0.04	0.48	0.40	0.01	0.04	0.05	0.03
U	0.12	0.07	0.14	0.09	0.31	0.08	0.39	0.04	0.01	0.24	0.28	0.20

The gabbros are strongly mylonitized with elongated clinopyroxene (Cpx) and fine-grained, recrystallized plagioclase (Figure 4a). The massive basalts or doleritic dykes show ophitic texture (or intergranular texture) with well-developed plagioclase laths and fine-grained Cpx (Figure 4b). Some pillow basalts are weakly altered with pilotaxitic texture (Figure 4c), and some are strongly altered by epidote and chlorite (Figure 4d). The peridotite is strongly serpentinized without olivine and pyroxene relics. Spinels are

Table 1c. Whole-Rock Major and Trace Element Compositions of Daqing Pasture and Wudaoshimen Ophiolites in the XIMAB

	Daqing Pasture Phiolite						Wudaoshimen Basalts		
	13XL-67	13XL-68	13XL-69	13XL-70	13XL-75	13XL-76	13LX01	13LX02	13LX03
Sample	SD	SD	SD	SD	SD	SD	PB	PB	PB
SiO_2	49.37	49.18	47.86	45.52	47.59	48.71	45.10	49.76	50.01
TiO_2	1.655	1.076	1.280	1.397	1.111	1.447	1.72	1.61	1.66
Al_2O_3	10.42	12.08	12.02	12.19	12.45	11.70	13.84	13.30	13.61
Fe_2O_3t	13.98	11.20	12.74	13.74	11.72	13.07	16.09	14.08	12.59
MnO	0.223	0.166	0.204	0.210	0.183	0.200	0.33	0.24	0.25
MgO	9.57	11.60	11.10	10.81	10.93	9.88	8.38	7.25	7.15
CaO	8.48	7.92	8.92	9.62	9.95	8.20	8.00	5.48	7.74
Na_2O	2.80	3.16	2.69	2.34	2.37	3.27	3.32	3.80	3.73
K_2O	0.18	0.06	0.16	0.13	0.25	0.06	0.31	0.20	0.51
P_2O_5	0.121	0.079	0.083	0.086	0.076	0.109	0.19	0.18	0.18
LOI	3.05	3.31	2.80	3.60	3.23	3.21	2.97	3.93	2.42
Mg#	61.5	70.7	67.0	64.7	68.5	63.8	54.8	54.5	57.0
				Trace Elements (ppm)					
Li	8.01	9.53	13.31	14.56	9.99	9.46	29.00	23.48	19.48
Sc	44.01	41.35	45.53	48.64	42.89	44.52	48.26	47.94	47.02
Ti	9,924	6452	7,671	8,377	6,661	8676	12,819	13,006	12,562
V	339.4	229.6	324.2	356.9	291.2	347.3	452.6	439.6	403.6
Cr	128.9	327.6	163.5	173.4	167.9	193.4	137.5	193.5	192.1
Co	39.92	28.42	39.87	36.65	33.85	41.84	54.61	47.58	47.00
Ni	46.33	55.81	60.31	53.36	53.99	55.52	65.96	129.74	148.22
Cu	48.22	46.89	54.35	56.96	46.26	64.97	52.16	64.20	63.80
Zn	110.26	69.35	96.45	101.59	74.44	97.77	122.98	155.98	129.48
Ga	12.63	11.48	17.18	18.93	14.93	16.33	20.41	17.36	16.66
Rb	4.46	0.37	3.25	1.72	3.26	0.37	11.63	5.96	9.46
Sr	83.6	120.9	129.0	120.2	173.8	116.8	170.6	172.7	250.0
Y	30.63	21.21	27.75	30.50	27.70	28.75	46.57	46.92	44.44
Zr	89.67	54.47	74.92	80.68	62.95	87.33	144.28	144.76	140.54
Nb	1.29	0.77	0.96	1.06	0.91	1.33	3.13	3.35	3.13
Cs	0.54	0.08	0.29	0.28	0.25	0.19	11.11	7.02	2.81
Ba	27.49	19.32	11.62	9.19	31.11	14.74	63.48	60.10	304.20
La	2.60	2.03	2.11	2.24	2.48	2.56	4.09	4.25	4.16
Ce	9.16	6.25	7.40	8.04	7.44	8.80	14.22	14.82	13.99
Pr	1.63	1.19	1.35	1.45	1.30	1.56	2.57	2.68	2.54
Nd	9.04	6.46	7.47	8.16	7.33	8.52	14.05	14.50	14.00
Sm	3.12	2.24	2.71	2.90	2.55	3.01	5.08	5.18	5.01
Eu	1.18	0.95	1.11	1.19	1.30	1.22	1.64	1.67	1.79
Gd	4.60	3.12	4.01	4.31	3.81	4.30	6.95	7.11	6.78
Tb	0.86	0.59	0.77	0.84	0.73	0.81	1.25	1.29	1.21
Dy	5.53	3.77	4.92	5.45	4.73	5.20	8.45	8.58	8.16
Ho	1.25	0.85	1.13	1.25	1.09	1.19	1.83	1.87	1.76
Er	3.79	2.55	3.47	3.78	3.26	3.53	5.35	5.43	5.12
Tm	0.52	0.36	0.48	0.53	0.45	0.51	0.78	0.80	0.74
Yb	3.32	2.28	3.15	3.40	2.83	3.23	5.06	5.07	4.79
Lu	0.52	0.35	0.49	0.52	0.43	0.50	0.76	0.77	0.70
Hf	2.69	1.58	2.25	2.46	1.99	2.59	3.31	3.35	3.23
Ta	0.09	0.05	0.07	0.07	0.06	0.25	0.19	0.22	0.22
Pb	0.84	1.74	1.22	0.98	0.37	0.51	0.93	1.04	0.68
Th	0.10	0.07	0.07	0.06	0.22	0.08	0.17	0.24	0.15
U	0.06	0.03	0.54	0.07	0.06	0.05	0.09	0.15	0.14

characterized by low TiO_2 (0.05–0.06 wt %) and relatively low $Cr^{\#}$ [100Cr/(Cr + Al) = 51.4–53.5] and plot in the abyssal peridotite field (Table S3 and Figure 5).

4.1.1. Major and Trace Elements

Four sheeted dyke, two pillow basalt and two gabbroic samples were selected for whole-rock major and trace element analysis (Tables 1a, 1b, 1c). The sheeted dyke samples have higher Al_2O_3 (17–19 wt %), lower Fe_2O_3t (7–9.68 wt %), and higher $Mg^{\#}$ [100Mg/(Mg + Fe^{2+}) = 66–71] than those of the two basaltic

samples. They are all tholeiitic and compositionally similar to N (normal)-type MORB with normal contents of SiO_2 (48–51 wt %), TiO_2 (0.81–1.33 wt %), MgO (6.9–8 wt %), and varying Cr and Ni. In the primitive mantle (PM) normalized multielement diagram, all sheeted dykes and pillow basalts show similar patterns to present-day N-type MORB (Figure 6a), except for variably enriched Cs, Rb, Ba, U, and Pb (not shown in the diagrams) and for a weak negative Zr-Hf anomaly in the sheeted dyke samples. All basaltic samples have strong enrichment of Sr with Sr/Sr* of 1.25–3.4. The two gabbroic samples have high CaO, MgO, low REE contents, and positive Sr (Sr/Sr* = 3.1–9.6) and Eu (Eu/Eu* = 1.1–2.1) anomalies (Figure 6a).

4.1.2. Formation Ages

One gabbro (13XL30) and one dolerite (sheeted dyke; see Figures 3a and 4b) (13XL31) samples were selected for zircon U-Pb dating. Zircons from the two samples are colorless and show rectangle or irregular shapes with long axes of 50–100 μm and length/width ratios of 1.2–1.5. The CL images display straight and wide oscillatory growth bands (Figures 7a and 7b), which are interpreted as typical features for zircons from mafic volcanic or gabbroic rocks [e.g., *Song et al*., 2010]. Zircons from sample 13XL30 show varying U (20–314 ppm) and Th (10–1221 ppm) with Th/U ratios of 0.49–3.89. Analyses of 17 zircon grains using SIMS yield apparent $^{206}Pb/^{238}U$ ages of 371–340 Ma, giving an intercept age of 356 ± 5 Ma on the TW diagram, which is consistent with the weighted mean age of 356 ± 5 Ma (mean square weighted deviate (MSWD) = 2.8) (Figure 8a).

Zircons from sample 13XL31 show variably low U (8–50 ppm) and Th (2–17 ppm) with Th/U ratios of 0.2–0.53. Twenty analyses yield apparent $^{206}Pb/^{238}U$ ages of (341–320 Ma) with a weighted mean age of 329 ± 3 Ma (MSWD = 1.7), and all the analyses form an intercept age of 331 ± 2 Ma (MSWD = 1.0) on the TW diagram (Figure 8b). The age data of the two samples suggest that the Xi-Ujimqin ophiolite formed in the Early Carboniferous (356–330 Ma).

4.2. Diyanmiao Ophiolite With Spilitic Pillow Basalt

The Diyanmiao ophiolite is located in the Diyanmiao area, ~15 km east of the Xi-Ujimqin ophiolite (Figure 1). It consists of serpentinized peridotite, cumulate gabbro, pillow basalt, and chert. Most gabbro samples are strongly altered by actinolite and prehnite with a few Cpx relics. Pillow basalts have been found in several localities around this area. The pillows show yellow to dark brown colors and are 20–100 cm long (Figures 3b and 3c). Vesicles are rare in the pillows, suggesting that the lava lacks fluids or was erupted under deep water. Calcite veins are common in many pillows. All the basaltic samples exhibit a spilite texture with long, skeletal or acicular intergrown crystals of albite + clinopyroxene, similar to the spinifex texture of komatiites (Figure 4e). Unknown phenocrysts can be observed as single crystals all altered into iron-rich pumpellyite. Spinel occurs as fine-grained, euhedral crystals both as phenocrysts and in the matrix. Mineral compositions analyzed using electron probe microanalyzer are given in Table S4. Plagioclase crystals are Na rich (with Ab = 80–95). Clinopyroxene (Cpx) is augite with high Al_2O_3 (5.25–6.10%), TiO_2 (0.96–1.63%), and Cr_2O_3 (0.29–0.86%). Jadeite component in the Cpx can reach up to 12.55–14.23 mol %. Spinels are characterized by relatively high MgO and Al_2O_3 and low Cr_2O_3 with $Mg^{\#}$ [$Mg/(Mg + Fe^{2+})$ = 0.61–0.63] and $Cr^{\#}$ [Cr/(Cr + Al) = 0.48–0.50]. In diagrams for spinels (Figure 5), they all plot in the MORB field.

4.2.1. Geochemical Composition

We selected two gabbroic and seven basaltic samples for major and trace element analysis (Tables 1a, 1b, 1c). All the pillow basalts are characterized by relatively low TiO_2 (0.83–1.45 wt %), low K_2O (0.02–0.14 wt %), high Na_2O (3.4–4.13 wt %), MgO (7.5–10.2 wt %), and $Mg^{\#}$ (69.5–71.7), and high compatible elements Cr and Ni. One pillow basalt sample (13XL55) shows an enriched trace element composition similar to E-MORB. The other six pillow basaltic samples resemble N-type MORB, depleted in immobile incompatible elements, such as Th, Nb, Ta, Zr, Hf, and REE (Figure 6b), and enriched in Cs, Rb, Ba, Sr, U, and Pb, suggesting strong seawater alteration.

The two gabbroic samples exhibit complicated compositions and have much lower concentrations of immobile trace elements than N-MORB.

4.2.2. Formation Age

One gabbro sample (13XL59) and one pillow basalt sample (13XL40, Figure 3b) were selected for zircon U-Pb dating. More than 100 zircon grains were recovered from the gabbro sample, and about 50 grains from the pillow basalt sample, of ~5 kg for each. Zircons from the gabbro sample (13XL59) are colorless, euhedral crystals with varying long axis (50–150 μm and length/width ratios of 1.2–2.5). CL images show dark to intermediate luminescence with straight and wide oscillatory growth bands (Figure 6c). Zircons from sample

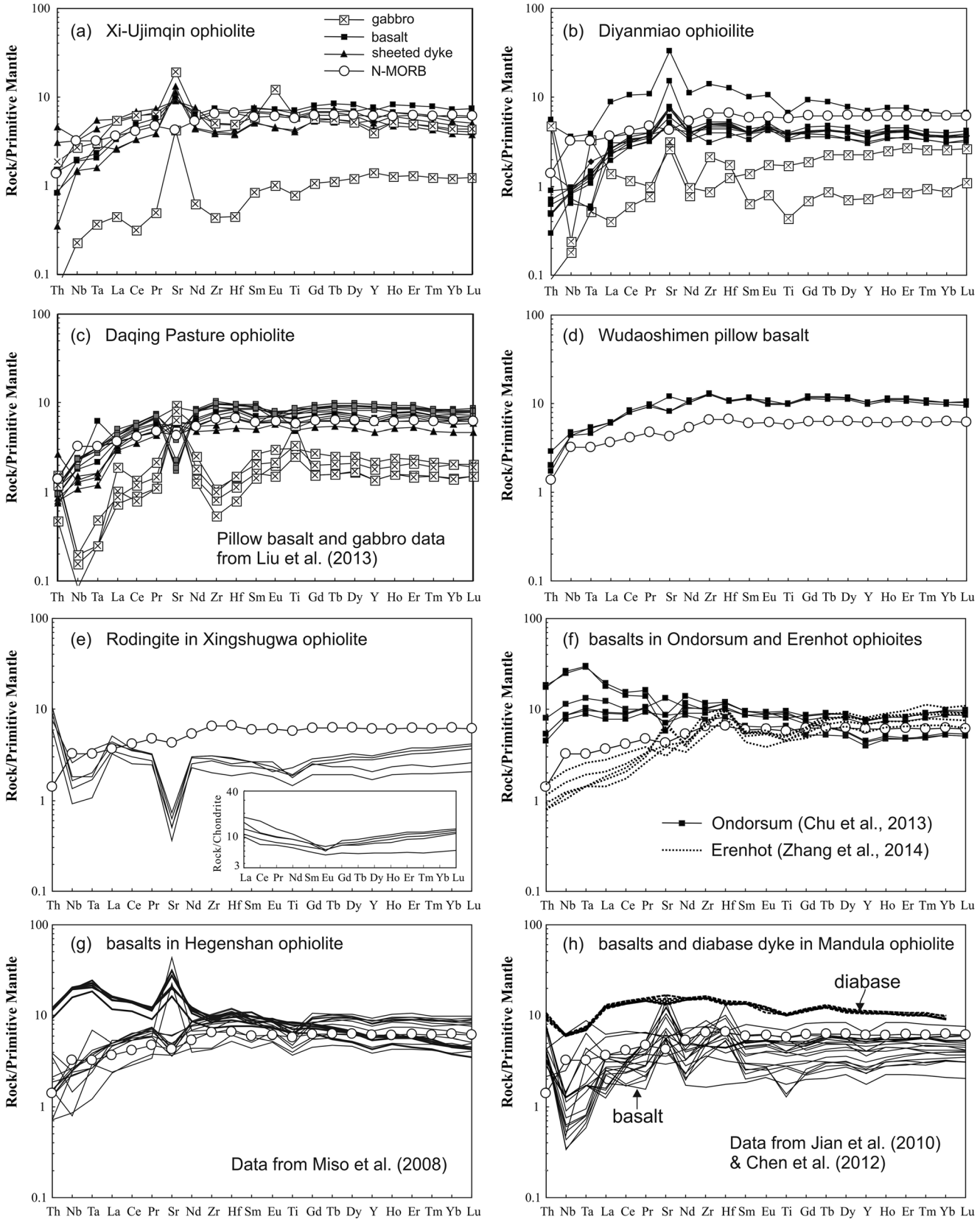

Figure 6. Primitive mantle-normalized multielement spidergrams for ophiolites from the XIMAB of the CAOB. Normalization values are from *Sun and McDonough* [1989]. Mobile elements, such as Cs, Rb, Ba, U, and Pb, are not shown.

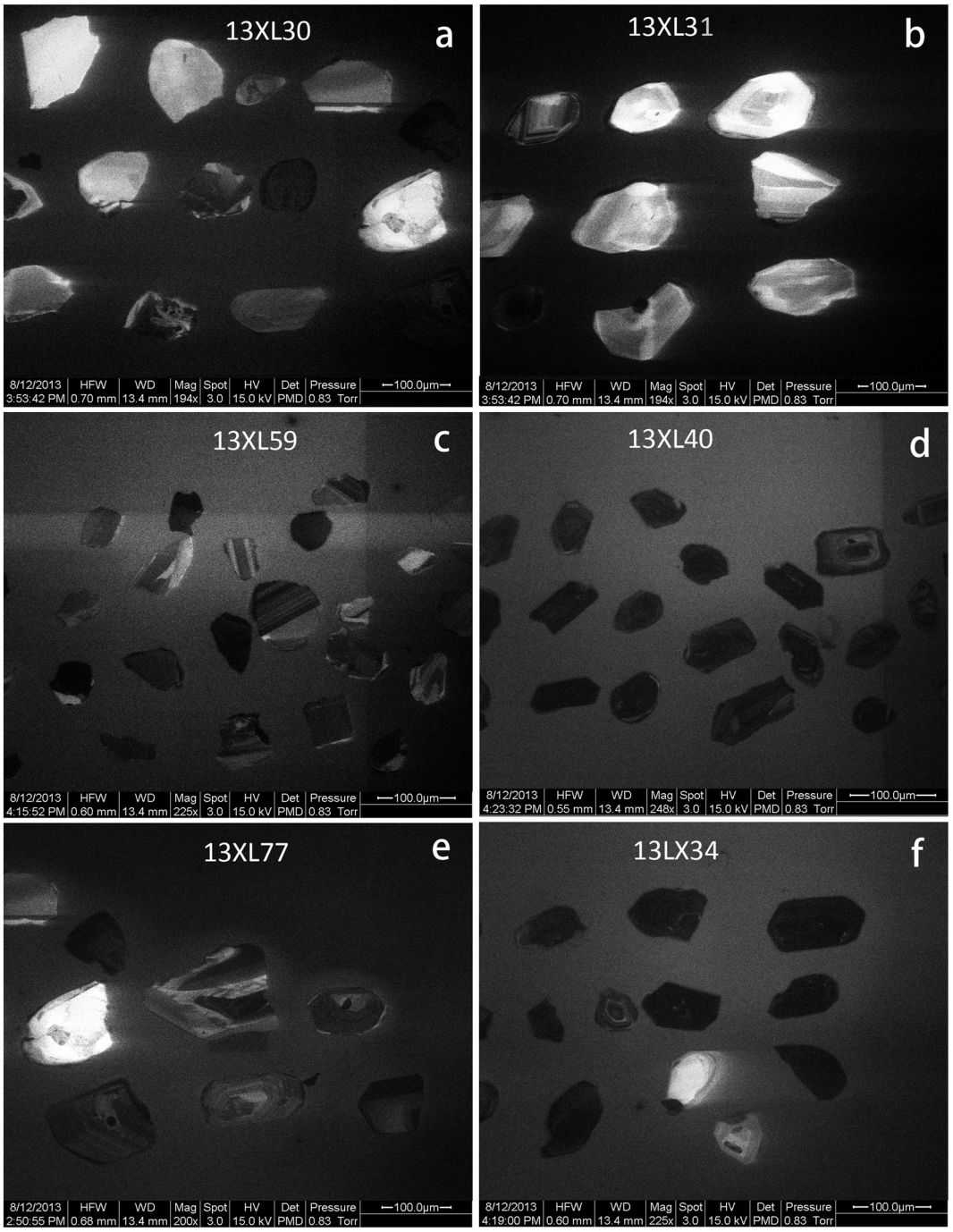

Figure 7. Cathodoluminescence (CL) images for zircons from gabbroic and basaltic samples in ophiolites from the XIMAB of the CAOB.

13XL59 show highly variable U (24–442 ppm) and Th (11–236 ppm) with Th/U ratios of 0.29–0.85. Eighteen analyses of 18 zircons yield apparent $^{206}Pb/^{238}U$ ages of 352–338 Ma with a weighted mean of 346 ± 2 Ma (MSWD = 1.1) (Figure 7c).

Zircons from the spilitic pillow basalt (13XL40) are small euhedral crystals with long axes less than 100 μm, dark luminescence, and weak or no growth bands (Figure 7d). Both U (212–902 ppm) and Th (191–1120 ppm) are much higher than those in zircons from the gabbroic samples with varying Th/U (0.54–1.24). Twelve analyses yield apparent $^{206}Pb/^{238}U$ ages of (321–295 Ma) with a weighted mean of 305 ± 4 Ma (MSWD = 2.0), which is

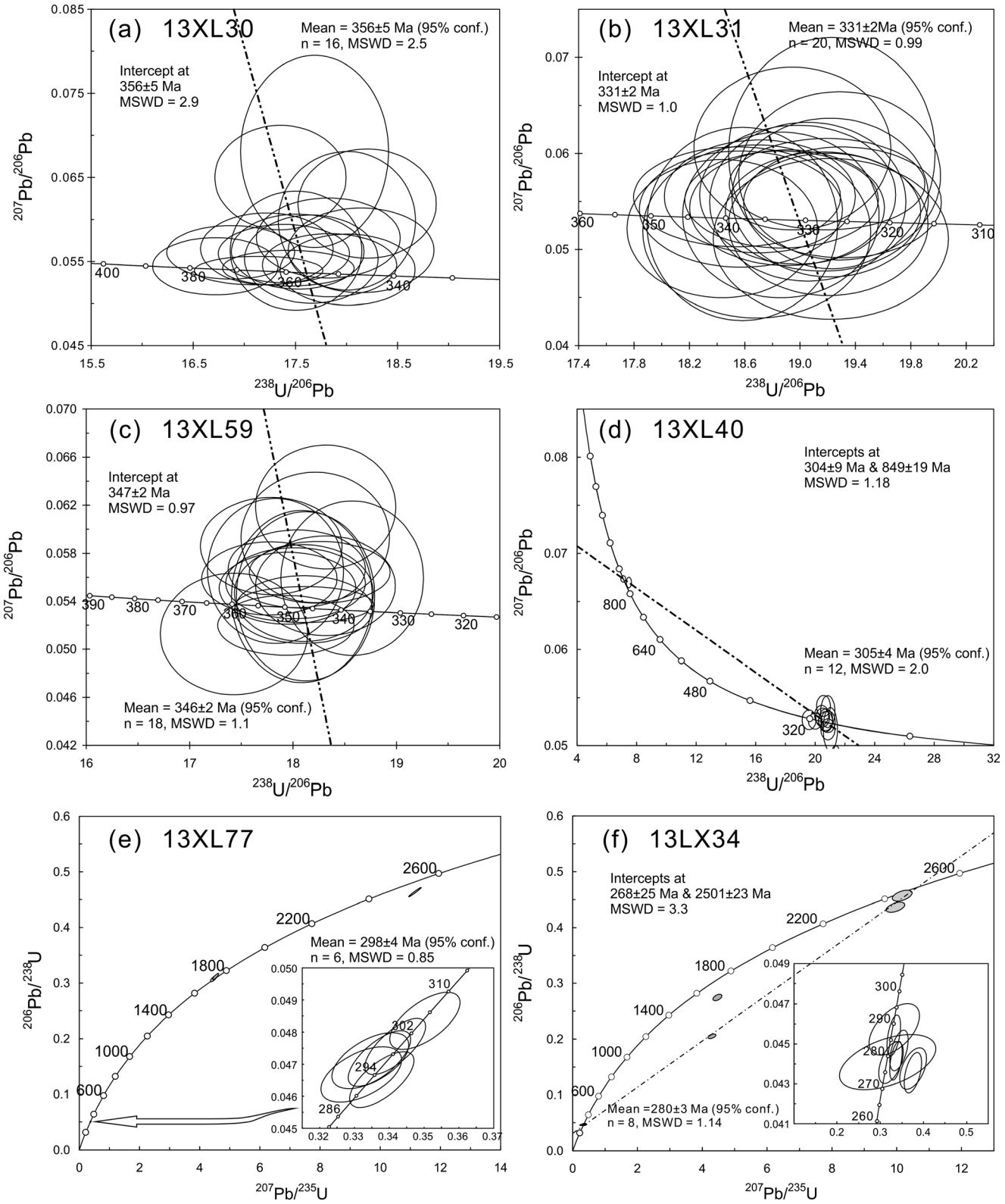

Figure 8. Concordant diagrams of zircon SIMS and LA-ICP-MS analyses for gabbroic and basaltic/doleritic samples in ophiolites from the XIMAB of the CAOB. (a and b) SIMS analyses for zircon from gabbro and dolerite (sheeted dyke?) in the Xi-Ujimqi ophiolite. (c) SIMS analyses for zircon from a gabbro in the Diyanmiao ophiolite. (d) SIMS analyses for zircon from a spilitic basalt in the Diyanmiao ophiolite. (e) SIMS analyses for zircon from a sheeted dyke in the Daqing pasture ophiolite. (f) LA-ICP-MS analyses for zircon from a rodingite in the Xingshuwa ophiolite.

Table 2. Sr-Nd Isotopic Data for Basaltic Rocks From Ophiolites in the Middle Part of the XIMAB

Sample	Rock	Rb	Sr	$^{87}Rb/^{86}Sr$	$^{87}Sr/^{86}Sr$	2σ	$I_{Sr}(t)$	Sm	Nd	$^{147}Sm/^{144}Nd$	$^{143}Nd/^{144}Nd$	2σ	$I_{Nd}(t)$	$\varepsilon_{Nd}(0)$	$\varepsilon_{Nd}(t)$
		(ppm)	(ppm)				(300 Ma)	ppm	ppm						
13XL-29	Xi-Ujimqi basalt	5.60	364.65	0.0434	0.706226	0.000017	0.706041	4.14	14.21	0.18504	0.513021	0.000019	0.512658	7.480	7.93
13XL-33	Xi-Ujimqi basalt	1.00	125.50	0.0225	0.705018	0.000013	0.704921	1.76	5.38	0.208048	0.513151	0.000019	0.512742	9.998	9.57
13XL-40	Diyanmiao basalt	1.35	156.38	0.0244	0.704962	0.000017	0.704858	1.79	5.37	0.21133	0.513118	0.000013	0.512703	9.360	8.81
13XL-43	Diyanmiao basalt	0.60	92.11	0.0185	0.705652	0.000019	0.705574	1.79	5.54	0.205357	0.513068	0.000015	0.512665	8.385	8.06
13XL-55	Diyanmiao basalt	2.19	688.81	0.0090	0.706247	0.000015	0.706209	4.43	15.17	0.185117	0.513052	0.000017	0.512688	8.077	8.53
13XL-66	Daqing basalt	25.69	260.09	0.2790	0.707201	0.000012	0.706010	3.83	13.79	0.176437	0.512910	0.000017	0.512563	5.297	6.08
13XL-69	Daqing basalt	3.25	128.97	0.0711	0.703661	0.000018	0.703358	2.71	7.47	0.230069	0.513176	0.000018	0.512725	10.502	9.23
13XL-75	Daqing basalt	3.26	173.80	0.0529	0.703873	0.000019	0.703647	2.55	7.33	0.220586	0.513134	0.000018	0.512701	9.684	8.78
13LX-32	Xingshuwa rodingite	0.58	45.39	0.0360	0.707082	0.000019	0.706997	2.26	7.76	0.18445	0.512742	0.000019	0.512380	2.028	2.50
13LX-33	Xingshuwa rodingite	0.05	70.94	0.0020	0.707069	0.000016	0.707064	1.24	4.79	0.164868	0.512745	0.000015	0.512421	2.083	3.30

interpreted to be the formation age of the pillow basalt (Figure 7d). Two analyses give 848 ± 12 Ma (concordant) and 808 ± 11 Ma (discordant), which may be zircon xenocrysts (Table 2).

4.3. Daqing Pasture Ophiolite

The Daqing pasture ophiolite outcrops are between Linxi and Xi-Ujimqin (Figure 1) and were first reported by *Liu et al*. [2013]. It occurs as thrusting slices on to the strongly deformed Permian strata (Figure 9). This ophiolite consists mainly of sheeted dykes (Figure 3d), pillow basalts, and chert (Figure 3e), i.e., the upper part of the ophiolite suite. The sheeted dykes are 0.3–0.6 m wide, and each has a clear one-sided chilled margin. They show ophitic texture with well-developed plagioclase laths and fine-grained Cpx (Figure 4f). Most pillow basalts are deformed and fractured to various extent, and the fresh sample shows pilotaxitic texture with orientated plagioclase laths and Cpx phenocrysts (Figure 4g). In fact, the foliated basalts, as termed by *Liu et al*. [2013], exhibit geochemical characters of cumulate gabbro with positive Eu, Sr anomalies, negative Nb-Ta-Ti anomalies, and much lower REE abundances than the pillow basalts. Zircons from two samples have been previously dated to give a mean age of 318–315 Ma [*Liu et al*., 2013].

All pillow basalts show geochemical characteristics of low-K tholeiite with normal abundances of SiO_2, Al_2O_3, TiO_2, Mg, and $Mg^{\#}$ (0.46–0.51). Except for variably enriched LILEs, U, and Pb, all samples are similar to present-day N-type MORB (Figure 4c). The sheeted dykes in this study also show low-K tholeiitic compositions but have higher MgO (9.57–11.60 wt %), $Mg^{\#}$ (Mg/(Mg + Fe) = 0.62–0.71), Cr (129–328 ppm), and Ni (46–60 ppm) than the pillow basalts. In contrast to the pillow basalts, the sheeted dykes have slightly low REE abundances but similar Chondrite-normalized REE patterns. In the PM-normalized multielement spidergrams (Figure 6c), the sheeted dykes exhibit more depleted Th, Nb, and Ta than the pillow basalts and the present-day N-type MORB.

Zircon separates from the sheeted dyke sample (13XL77, Figure 3d) are colorless, euhedral, or broken grains with varying long axial length (50–100 μm). CL images display straight and wide oscillatory growth bands, similar to zircons from gabbroic samples (Figure 7e). Zircons have high U (335–460 ppm) and Th (124–270 ppm) with Th/U ratios of 0.37–0.59. Six zircons yield apparent $^{206}Pb/^{238}U$ ages of 304–293 Ma, giving a weighted mean of 298 ± 4 Ma (MSWD = 0.85). One zircon gives a $^{207}Pb/^{206}Pb$ age of 2603 ± 5 Ma, and the other two give 1719 ± 21 Ma and 1724 ± 16 Ma (Figure 8e), which are most likely contaminated from the NCC basement.

Together with the ages of gabbroic samples determined by *Liu et al*. [2013], our age data indicate that the Daqing ophiolite was formed from 320 to 300 Ma.

4.4. Wudaoshimen Pillow Basalts

A thick layer of pillow basalts (>500 m) occurs in the Wudaoshimen area, 62 km west of Linxi (Figure 1). The basalts

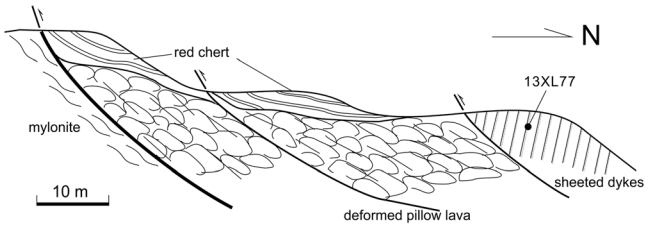

Figure 9. Field section showing occurrence of the Daqing pasture ophiolite as southward thrusting slices.

all occur as pillows (Figure 3f) and show ophitic (or intergranular) texture of euhedral lath-shaped plagioclase crystals and fine-grained Cpx (Figure 4h). Red radiolarian chert is occasionally observed as lenses between the pillows [*M. Wang et al.*, 2014]. Fine-grained pyroclast-rich sedimentary layers cover the pillow lava. Previous studies [*He and Shao*, 1983; *Li*, 1987] suggested that they are Early Paleozoic ophiolites without age data. Recently, *Y. Y. Wang et al.* [2014] reported a reliable zircon age for a pillow basalt with ophitic texture; analysis of 15 zircons (exhibiting CL features of mafic magma) gave a concordant weighted mean age of 277 ± 3 Ma, suggesting that the basalts formed in the Early Permian.

Geochemical analyses of three pillow basalt samples show tholeiitic compositions with normal contents of SiO_2 (45–50 wt %), TiO_2 (1.6–1.7 wt %), MgO (7.15–8.38 wt %), high Na_2O (3.32–3.80 wt %), and low K_2O (0.20–0.51 wt %), similar to present-day N-type MORB. They have higher concentrations of incompatible elements than, but similar patterns to, the present-day N-type MORB (Figure 6d).

4.5. Xingshuwa Ophiolite

The Xingshuwa ultramafic-mafic massif is located in the southern part of the CAOB, ~40 km south of Linxi (Figure 1). It consists of peridotite (mostly harzburgite), pyroxenite, gabbro, diabase dykes, deformed/metamorphosed basalt, and chert (Figure 3g). *Wang and Pan* [1997] reported radiolarians of middle Permian from the red-colored chert. Podiform chromitite was occasionally observed in the peridotite. All the peridotite samples are strongly serpentinized without relict olivine. Orthopyroxenes occur as pseudomorphs and deformed (Figure 4i). Fresh spinel crystals (Figure 4i) are characterized by low TiO_2 (0.02–0.06 wt %) and high Cr# [100Cr/(Cr + Al) = 60.7–75.2] (Table S3); they all plot in the fore-arc peridotite field (Figure 5a).

Rodingite occurs as veins of 10–50 cm wide within the peridotite (Figure 3h) and consists of high-Ca minerals such as prehnite, epidote, tremolite, vesuvianite, grossular, and diopside with fine-grained zircons (Figure 4j). Original euhedral spinel crystals survive in the matrix and have compositional characters of high Cr_2O_3 (47.2–51.3 wt %), low Al_2O_3 (13.0–16.8 wt %), and MgO (1.3–11.9 wt %) with $Cr^{\#}$ [100Cr/(Cr + Al)] of 65.6–70.8 (Table S3), plotting in the arc field (Figure 5b). The rodingite veins are compositionally characterized by high CaO (17.4–30.5 wt %), $Mg^{\#}$ (64–83), Cr (230–2834 ppm), Ni (146–1173 ppm), low TiO_2 (0.2–0.6 wt %), and extremely low Na_2O and K_2O. All the samples show wide "V-shaped" REE patterns with right-tilted LREE (La to Eu) and left-tilted HREE (Eu to Lu), and strongly enriched Th, U, Pb, and depleted Rb, Sr, Nb, Ta, and Ti in the primitive mantle-normalized multielement diagrams (Figure 6e), suggesting intensive fluid alteration.

Zircon grains were separated from one rodingite sample 13LX34 (Figure 3h). They are colorless, euhedral crystals with dark luminescence and weak oscillatory growth bands (Figure 7f). U-Pb analyses for eight zircons by LA-ICPMS yield apparent $^{206}Pb/^{238}U$ ages from 288 to 275 Ma with a weighted mean of 280 ± 3 Ma (MSWD = 1.14). These zircons have high U (505–3722 ppm) with Th/U ratios of 0.15–0.87. Three zircons form a discordant line with an upper intercept at 2501 ± 23 Ma, and one zircon yields a discordant $^{207}Pb/^{206}Pb$ age of 1931 ± 19 Ma (Figure 8f). These zircons are most likely derived from the Precambrian basement of the NCC.

The occurrence of rodingite veins in the Xingshuwa peridotite massif suggests seafloor alteration. However, the high $Cr^{\#}$ of spinels in the rodingite indicates that they are different from the abyssal peridotite [*Dick and Bullen*, 1984; *Niu and Batiza*, 1997], and all plot in the arc (island arc magmas) field in the spinel TiO_2-Al_2O_3 diagram (Figure 5) of *Kamenetsky et al.* [2001]. We conclude that the Xinshuwa ophiolite complex should be formed in an arc, fore-arc, or back-arc setting.

4.6. Ondorsum Ophiolite

The Ondorsum ophiolite suite is located in western XIMAB, ~ 20 km north of Ondorsum (Figure 1). It has been studied by different authors for more than 20 years [*Hsü et al.*, 1991; *Xiao et al.*, 2003; *Miao et al.*, 2007; *Chu et al.*, 2013]. *Miao et al.* [2007] defined it to be a member of the Ondorsum-Xar Moron ophiolite belt, which

contains several ophiolite blocks, including the Ondorsum, Kedanshan, Banlashan, and Xinshuwa, along the southern portion of the CAOB.

The Ondorsum ophiolite consists predominantly of thick layered pillow lavas with minor sheeted dykes. Gabbro has not been found in this ophiolite block. Carbonatized peridotite occurs as a dyke-like block of 2–5 m wide and hundreds of meters long. The sheeted dyke unit is composed of 100% dykes (Figure 3i), but one-way chilled margins are ambiguous. The pillow lavas are deformed showing varying width/length ratios (Figure 3j). Red-colored radiolarian chert can be observed as thin layers within the pillow lavas (Figure 3k).

Geochemical analyses (data from *Chu et al*. [2013]) show that basalts from the Ondorsum ophiolite are tholeiitic with high TiO_2 (1.3–3.2 wt %), Na_2O (2.5–5.3 wt %), and low K_2O (0.01–0.57 wt %). In the Nb/Y versus Zr/Ti diagram [*Winchester and Floyd*, 1977], these basalts distribute from the subalkaline basalt field to the alkaline basalt field. In the multielement diagram, these volcanic rocks exhibit patterns resembling present-day E-MORB (Figure 6f), except for the strong U enrichment.

The formation age of the Ondorsum ophiolite was poorly constrained because of the difficulty of dating fine-grained basalts. *Miao et al*. [2007] reported analyses for three zircon grains from a pillow basalt sample, giving an age of ~ 260 Ma. *Chu et al*. [2013] reported zircon ages of six pillow basalt samples; five samples with 117 zircon grains yielded clusters of ages from 237 Ma to 2734 Ma, and one sample yielded a reasonable weighted mean age of 246 ± 3 Ma (n = 12, MSWD = 1.9). These ages suggest that the Ondorsum ophiolite most likely formed in the Late Permian to Early Triassic.

4.7. Other Ophiolite Suites

4.7.1. Ophiolite Complexes in the Hegenshan Region

The Hegenshan region is located in the northern part of the Xing'an-Inner Mongolia accretionary belt (Figure 1). This region contains four large ultramafic-mafic massifs plus several small ones with massive/podiform chromitite ore deposits (Figure 1) and has been classified into the Eranhot-Hegenshan ophiolite belt, which was considered to be the best representation of the Paleo-Asian Ocean [e.g., *Bao et al*., 1994; *Nozaka and Liu*, 2002; *Miao et al*., 2008; *Jian et al*., 2010, 2012; *Xiao et al*., 2009a]. The Chaogenshan-Hegenshan massifs in the southwest consist of serpentinized harzburgite and lherzolite, cumulate gabbro and anorthosite, greenschist facies metamorphosed basalts, and diabase and anorthosite dykes [*Robinson et al*., 1999; *Miao et al*., 2008; *Jian et al*., 2010]. Geochemical analyses show that metabasalts and mafic dykes have features of both N-MORB and E-MORB [*Robinson et al*., 1999; *Miao et al*., 2008] (Figure 6g). Sensitive high-resolution ion microprobe (SHRIMP) analyses for zircons from two gabbro samples gave weighted mean ages of 298 ± 9 Ma, 252 ± 9 Ma, and 295 ± 15 Ma, respectively, whereas zircons from a granodiorite dyke that intruded the ultramafic massif gave a weighted mean age of 244 ± 4 Ma [*Miao et al*., 2008]. However, *Jian et al*. [2012] reported zircon SHRIMP analyses from six gabbroic samples in the Chaogenshan-Hegenshan massifs, and all samples yielded complicated ages ranging from 500 Ma to 125 Ma with peaks at 135 Ma, 176 Ma, 235 Ma, 271 Ma, and 306 Ma. CL images of the analyzed zircons also show a complex inner structure, implying that they may come from multiple sources, but we cannot rule out the possibility of contamination during zircon separation.

The Xiaobaliang peridotite massive, next to the Hegenshan massif to the northeast, consists of a major ultramafic body with gabbro and plagiogranite dykes. No cumulate gabbro nor pillow basalts were observed. *Jian et al*. [2012] reported a zircon SHRIMP age of 354 ± 7 Ma for microgabbro and 333 ± 4 Ma for plagiogranite. The Wusnihei peridotite massif in the northeast segment of the ophiolite belt, as described by *Jian et al*. [2012], is similarly dominated by serpentinized lherzolite, with subordinate harzburgite, dunite and pyroxenite, and gabbroic (gabbro, troctolite, and anorthosite) dykes. Zircons from a volcanic breccia gave a weighted mean age of 300 ± 2 Ma [*Jian et al*., 2012].

4.7.2. Eastern Erenhot Ophiolite

The Eastern Erenhot ophiolite is located ~60 km east of the Erenhot city, near the China-Mongolia border (Figure 1). It has been recognized as one of the fragments of the Erenhot-Hegenshan ophiolite belt [*Liang*, 1994; *Robinson et al*., 1999] and recently studied by *Z. Zhang et al*. [2015]. This ophiolite is composed of serpentinized ultramafic rocks with subordinate gabbros, mafic lavas, red-colored radiolarian chert, and minor plagiogranite dykes. The basaltic rocks show characteristics of N-MORB affinities with depleted Th, Nd, Ta, and LREEs (Figure 6f). Zircons from two gabbro samples and one plagiogranite sample yielded weighted mean ages of 354.2 ± 4.5 Ma, 353.3 ± 3.7 Ma, and 344.8 ± 5.5 Ma, respectively [*J. Zhang et al*., 2015].

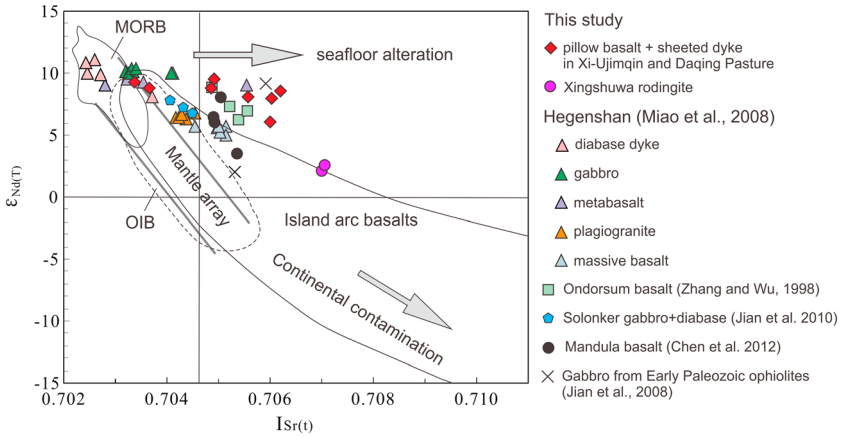

Figure 10. Sr-Nd isotopic compositions of various rocks from ophiolite complexes in the Xing'an-Inner Mongolia accretionary belt of the CAOB. Data are from *Miao et al.* [2008], *Zhang and Wu* [1998], *Jian et al.* [2010], *Chen et al.* [2012] and this study.

4.7.3. Mandula Ophiolitic (?) Complex in the Solonker Belt

The Mandula ophiolitic (?) complex is located in the Solonker belt, or Solonker suture of *Xiao et al*. [2003], in the western section of the XIMAB (Figure 1). *Jian et al*. [2010] distinguished four geological units from south to north: (1) the Hugiert-Chaganhadamiao volcanic-plutonic sequence with pillow and massive volcanic and plutonic rocks, (2) the Mandula fore-arc mélange, (3) mid-Permian alluvial sediments, and (4) Early Permian bimodal volcanic rocks. Lithologies associated with the ophiolite in the Mandula region are fragments of serpentinized peridotite, gabbro, diabase dykes, plagiogranite, and red chert.

Geochemical analyses (data from *Jian et al*. [2010] and *Chen et al*. [2012]) show that the diabase dykes have enriched trace element compositions of E-MORB affinity, except for an obvious Nb-Ta negative anomaly relative to Th and La (Figure 6h). All other basalts exhibit characteristics of IAT with strong depletion of Nb and Ta relative to Th and La and strongly enriched Sr (Sr/Sr* = 1.03–5.98) (Figure 6h). *Jian et al*. [2010] suggested that the Mandula ophiolite complex formed in an environment of suprasubduction zone (SSZ), whereas *Chen et al*. [2012] argued that they formed in a rift or a small oceanic basin. Zircon U-Pb analysis by SHRIMP for two diabase samples gave weighted mean ages of 274.4 ± 2.5 Ma and 252.5 ± 2.3 Ma [*Jian et al*., 2010], respectively. *Chen et al*. [2012] reported a zircon weighted mean age of 278.5 ± 3.0 Ma from gabbro and 273.7 ± 1.0 Ma for a basalt. Therefore, the Mandula ophiolite was formed in Permian times.

4.8. Sr-Nd Isotopes

All the Sr-Nd isotopic data of ophiolites in the XIMAB, including those in the literature and newly analyzed in this study, are presented in Figure 10. Rock types include (cumulate) gabbro, diabase dyke, basalt, and plagiogranite, and all have $\varepsilon_{Nd}(t) > +2$. The gabbro and basaltic rocks from the Hegenshan ophiolite complex have highest $\varepsilon_{Nd}(t)$ and lowest I_{Sr}; most plot in the field of present-day MORB, suggesting that they are comparable to the Sr-Nd isotopic compositions of major modern ocean crust. Rodingites from the Xingshuwa ophiolite complex have the lowest $\varepsilon_{Nd}(t)$ (+2.5–+3.3) and highest I_{Sr} (t) (~0.707). The deviation of I_{Sr} from the mantle array reveals strong seafloor alteration.

All the samples show a rough trend of increasing enrichment from north (Hegenshan region) to south (Xingshuwa region), suggesting an increase of continental contamination from oceanic crust to island arc or back-arc setting.

5. Discussion

5.1. Spatiotemporal Variation of Ophiolites in the XIMAB

As shown in Figure 1, ophiolite blocks/massifs are scattered in a ~400 km wide zone in the XIMAB. Such a wide zone has been suggested to have resulted from continuous accretion by multistage trench retreat or multiple subduction zones in the same time [e.g., *Windley et al*., 2007; *Xiao et al*., 2008, 2009a]. Several researchers have tried to give a clear subdivision of tectonic units for this wide zone on the basis of the ophiolite distribution

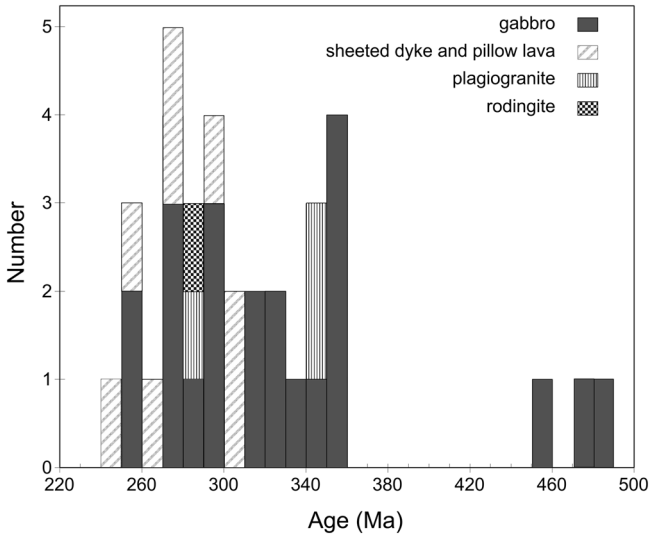

Figure 11. Distribution of zircon U-Pb ages from ophiolites in the XIMAB of the CAOB. Data are from *Liu et al*. [2003], *Miao et al*. [2007, 2008], *Jian et al*. [2008, 2010, 2012], *Chen et al*. [2012], *Chu et al*. [2013], *Y. Y. Wang et al*. [2014], *S. Zhang et al*. [2014], and this study.

[*Miao et al*., 2007; *Jian et al*., 2010, 2012; *Li*, 2006; *Xiao*, 2009a; *Xu et al*., 2013, 2014], but these subdivisions have been based on limited data with limited compositional variations in time and space. Combining previous studies [e.g., *Xiao et al*., 2003, 2009a; *Jian et al*., 2010; *Miao et al*., 2007, 2008; *Z. Zhang et al*., 2015], two ophiolite belts, i.e., the Erenhot-Hegenshan belt in the north and Solonker-Linxi belt in the south, which are separated by the Baolidao-Xilinhot metamorphic-volcanic-plutonic belt (or arc complex) [e.g., *Chen et al*., 2009], have been recognized.

Figure 11 and Table 3 show all the reliable zircon U-Pb ages from the literature and this study. Of all the ophiolite complexes in this belt, only two have been determined to be formed in the Early Paleozoic. Zircons from cumulate gabbro/metagabbro in the Tulinkai ophiolitic complex (Figure 1) give two $^{206}Pb/^{238}U$ weighted mean ages of 457 ± 4 Ma and 480 ± 2.4 Ma [*Miao et al*., 2007; *Jian et al*., 2008], and cumulate gabbro in the Sonitzouqi complex (Figure 1) gives a weighted mean age of 483 ± 2 Ma [*Jian et al*., 2008]. There is a ~90 Myr gap between 450 Ma and 360 Ma for which no ophiolite complex has been identified. Ophiolite complexes appeared again at ~360 Ma, the beginning of Carboniferous, and lasted continuously until ~245 Ma, the end of Early Triassic. These ages form two major peaks at 360–340 Ma (peak at 349 Ma) and 300–270 Ma (peak at 286 Ma). This ~90 Myr gap of the ophiolite in this belt indicates two individual spreading or preservation events of ocean crust in the long history of the Paleo-Asian Ocean, which is consistent with the relevant arc magmatism in the XIMAB of the CAOB (see below).

5.2. Formation Environments of Ophiolites: Subduction or No Subduction?

The tectonic environment of ophiolite emplacement has been a long-standing matter of debate [e.g., *Miyashiro*, 1975; *Pearce et al*., 1984; *Pearce*, 2003, 2008; *Pearce and Robinson*, 2010; *Dilek et al*., 2007; *Dilek and Furnes*, 2011]. *Dilek and Furnes* [2011] simply subdivided ophiolites into "subduction-related" and "subduction unrelated" and indicated that their lithological and geochemical characteristics vary with spreading rate, proximity to plumes or trenches, mantle temperature, mantle fertility, and the availability of fluids. Generally, troctolite can be crystallized in dry conditions [*Gaetani et al*., 1993; *Niu et al*., 1999] and is common in modern ocean crust generated in both fast- and slow-spreading ridges [e.g., *Arai and Matsukage*, 1996; *Drouin et al*., 2010; *Gillis et al*., 2014], whereas wehrlite occurs in hydrous conditions and is common in subduction-related setting. These two rock types, which may occur in the cumulate section of the ophiolites, are effective indicators of their formation environments [e.g., *Pearce*, 2003, 2008].

Most ophiolites in the studied region are dismembered or altered by late metamorphism and deformation, without well-preserved cumulate sections. The sheeted dykes in some ophiolite complexes as described above, on the other hand, should represent the relics of the spreading ridge, which convincingly demonstrate that they must be generated in the spreading center of either an ocean or a back-arc basin.

The depleted Nd isotopic data ($\varepsilon_{Nd}(t)$ +5–+11) for most ophiolites (except for rodingites in the Xingshuwa ophiolite and the gabbro in the Early Paleozoic Tulinkai ophiolite), similar to isotopes of the EPR basalts ($\varepsilon_{Nd}(t)$ +7 ~ +12) [*White et al*., 1987], indicate that they were derived from the depleted mantle source with subsequent seafloor weathering/alteration (Figure 9), which exclude the possibility of marginal ophiolites forming in an rift or a young ocean basin (e.g., Red Sea-type ocean-continent transitions) [*Dilek and Furnes*, 2011]. All the basaltic rocks, including pillow lavas and sheeted and isolated dykes in the ophiolites, are tholeiitic in major element compositions, and most are N-type MORB with depleted REE patterns [$(La/Sm)_N < 1$

Table 3. Summary on Reliable Zircon Ages of Ophiolites in the XIMAB

Ophiolite	Dating Rock	Age (Ma)	Reference
	Early Paleozoic Ophiolite		
Tulinkai	cumulate gabbro	457 ± 4	*Miao et al.* [2007]
	metagabbro	479.6 ± 2.4	*Jian et al.* [2008]
Sonitzuoqi	cumulate gabbro	482.5 ± 1.7	*Jian et al.* [2008]
	Erenhot-Hegenshan-Xi-Ujimqin Ophiolite Belt		
Hegengshan	gabbro	298 ± 9	*Miao et al.* [2008]
	leucogabbro	252 ± 9	*Miao et al.* [2008]
	leucogabbro	295 ± 15	*Miao et al.* [2008]
Xiaobaliang	gabbro	354 ± 7	*Jian et al.* [2012]
	gabbro	333 ± 4	*Jian et al.* [2012]
Wusnihei	basaltic rock	300.3 ± 2	*Jian et al.* [2012]
Xi-Ujimqin	gabbro	356 ± 4.7	This study
	sheeted dyke (?)	329 ± 3	This study
Diyanmiao	gabbro	346 ± 2.4	This study
	pillow basalt	304 ± 4	This study
Daqing	basalt/gabbro	318 ± 3	*Liu et al.* [2013]
	basalt/gabbro	315 ± 4	*Liu et al.* [2013]
	sheeted dyke	299 ± 4	This study
Eastern Erenhot	gabbro	354 ± 3	*S.-H. Zhang et al.* [2014]
	gabbro	353.3 ± 3.7	*S.-H. Zhang et al.* [2014]
	plagiogranite	344.8 ± 5.5	*S.-H. Zhang et al.* [2014]
Xilin Hot	gabbro	323 ± 5	*Jian et al.* [2007]
	gabbro	280 ± 0	*Jian et al.* [2007]
	Solonker-Linxi Ophiolite Belt		
Solonker	gabbro	297 ± 2	*Jian et al.* [2010]
	diabase dyke	252.5 ± 2.3	*Jian et al.* [2010]
Ondorsum	Wulangou	260 ± 5	*Miao et al.* [2008]
	Wulangou	246 ± 4	*Chu et al.* [2013]
Xingshuwa	rodingite	280 ± 3	This study
Banlashan	cumulate gabbro	256 ± 3	*Miao et al.* [2008]
Solon Oba	cumulate gabbro	279 ± 10	*Miao et al.* [2007]
Mandula	gabbro	278.5 ± 3	*Chen et al.* [2012]
	basalt	274 ± 1	*Chen et al.* [2012]
	diabase dyke	274.4 ± 2.5	*Jian et al.* [2010]
	gabbro	284 ± 4	*Jian et al.* [2010]
	plagiogranite	288 ± 6	*Jian et al.* [2010]
Wudaoshimen	pillow basalt	277 ± 3	*M. Wang et al.* [2014]

and $(La/Yb)_N < 1$], with the exception of enriched E-MORB-type basalts in the Ondorsum ophiolite and Hegenshan ophiolite (Figure 12a). In the Nb/Th versus Nb/Ta diagram (Figure 12b), most basaltic samples have higher-than-primitive mantle (PM) Nb/Th ratios and are comparable with basalts from the modern Eastern Pacific Rise. Basalts from the Mandula ophiolite (280–250 Ma) and rodingites from the Xingshuwa ophiolite (280 Ma) have extremely low Nb/Th and Nb/La ratios, suggesting contamination by continental crust and/or subduction zone fluids.

In the Nb-Zr-Y discrimination diagram [*Meschede*, 1986], most basaltic rocks plot in the N-MORB field; some plot in the E-MORB and WPT fields (Figure 12c). However, in the Th-Hf-Ta diagram of *Wood* [1980] (Figure 12d) and Th/Yb versus Ta/Yb diagram (Figure 12e), basalts from the Mandula ophiolite and rodingites from the Xingshuwa ophiolite exhibit evolved Th relative to Ta, Hf, and HREEs and plot in CAB and IAT fields associated with back-arc environments, suggesting that subduction zone fluids may have interacted with the sources of these basaltic rocks. In the Cr-Y diagram (Figure 12f), most data plot in the MORB field, while basalts from the Mandula ophiolite plot in the IAB field and some rodingites from the Xingshuwa ophiolite fall in the boninite field.

In summary, on the basis of whole-rock chemical and Sr-Nd isotopic compositions, we conclude that most ophiolite complexes in the XIMAB of the CAOB, such as those from Eastern Erenhot (360–350 Ma), the Hegenshan-Xiaobaliang (350–295 Ma), the Xi-Ujimjin and Diyanmiao (360–300 Ma), the Daqing pasture (320–300 Ma), and the Ondorsum (~260–245 Ma), are most likely subduction unrelated and comparable to the modern fast-spreading Eastern Pacific Rise (EPR). The Mandula ophiolite (280–250 Ma) in the western

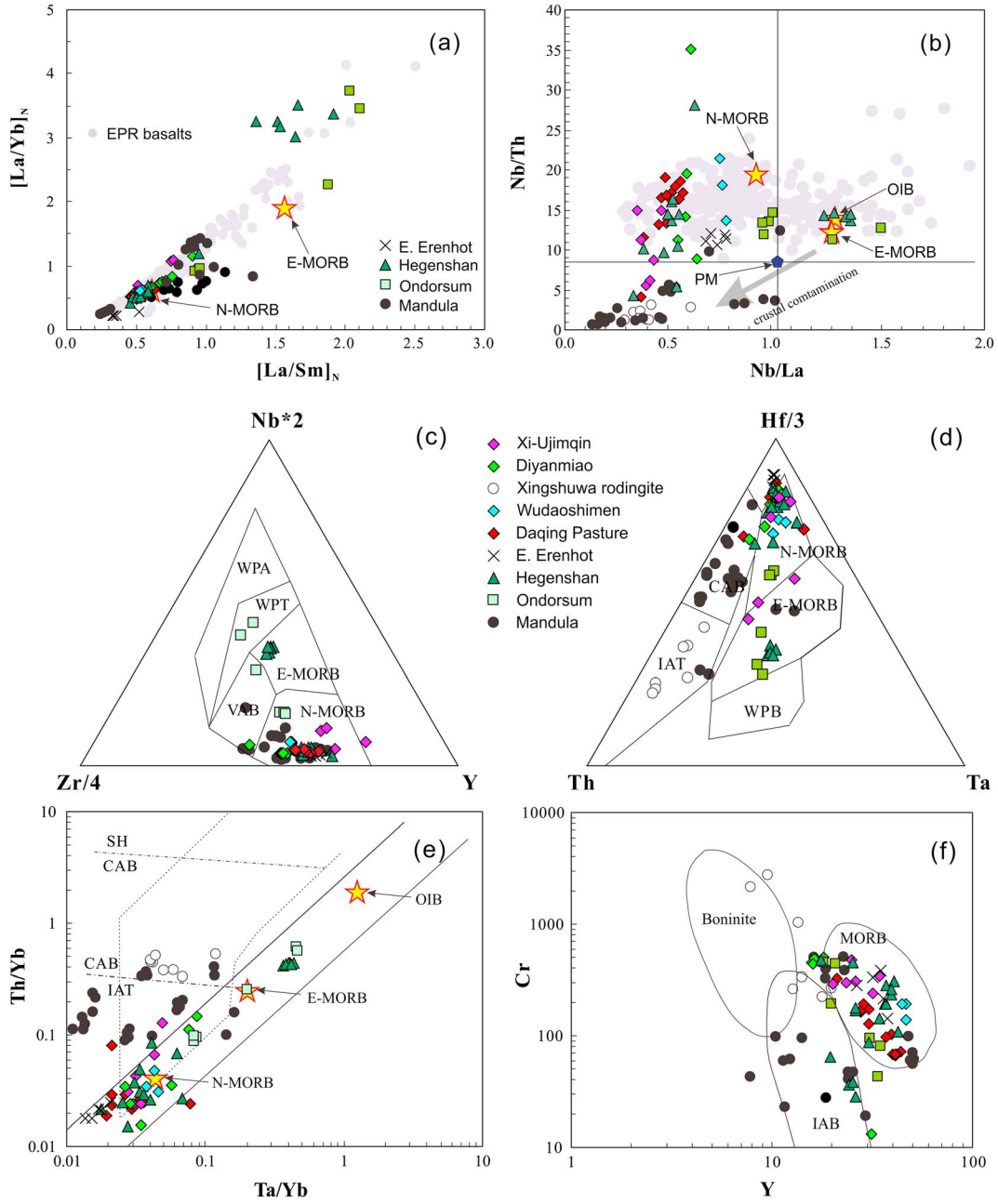

Figure 12. Discrimination diagrams for ophiolites from the XIMAB of the CAOB. See text for details. Data for the Daqing pasture ophiolite are from *Liu et al.* [2013] and this study, Eastern Erenhot from *J. Zhang et al.* [2015], Hegenshan ophiolite from *Miao et al.* [2008], Ondorsum from *Chu et al.* [2013], and Mandula from *Chen et al.* [2012]. Other data are from this study. EPR (Eastern Pacific Ridge) basalts are from *Niu and Hekinian* [1997], *Niu et al.* [1999, 2001, 2002], *Niu and O'Hara*, 2009, and *Regelous et al.* [1999]. The values for N-MORB, EMORB, OIB, and PM (primitive mantle) are from *Sun and McDonough* [1989].

section of the Solonker-Linxi belt and the Xingshuwa ophiolite (280 Ma) in the eastern section of the Solonker-Linxi belt show clear geochemical signatures of a suprasubduction zone (SSZ) setting. These subduction-related ophiolites suggest that back-arc extension occurred in the southern part of the orogen, which, in turn, requires southward oceanic subduction started at least in the Early Permian (~280 Ma).

Nevertheless, ophiolites, no matter in what environment they occur, should represent the existence of a disappeared, medium- to large-scale ocean(s) that evolved from the beginning of the Carboniferous to the

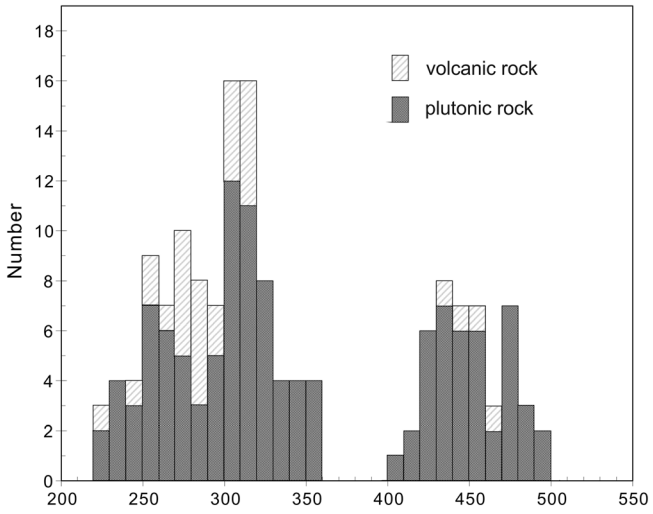

Figure 13. Age distribution of plutonic and volcanic rocks in the XIMAB sector of the CAOB. Data are from *Xu et al.* [2014, 2015, and references therein], with additions from *Li et al.* [2007], *S.-H. Zhang et al.* [2010], *Cao et al.* [2012, 2013], *Hu et al.* [2015], *Li et al.* [2014], *Fan et al.* [2014], and *Li et al.* [2015].

Early Triassic, as well as back-arc basins related to seafloor subduction, in the CAOB. It is worthy to note that although the ophiolites are dispersed in a vast area, they should belong to an individual ocean system, and we *must* not say that each ophiolite would represent an ocean or sea basin, the so-called "immature ocean," "Red Sea-type ocean," and "multiisland ocean," as interpreted in some literature. This wide ophiolite belt also implies that the CAOB is a type of accretionary orogen without intensive collision and mountain building between the convergent continents.

5.3. Spatiotemporal Distribution of Magmatism: Two Cycles of Accretionary Orogeny in the CAOB

Xu et al. [2014] examined the statistics of all the available magmatic ages for the Xing'an-Inner Mongolia belt of the CAOB [see *Xu et al.*, 2014, Figures 3 and 4], excluding Mesozoic (Jurassic to Cretaceous) magmatic overprinting. Plotting all the reliable zircon U-Pb ages on the histogram (Figure 13), we distinguish two epochs of magmatism, which coincide well with the age distribution of the ophiolites (Figure 11).

The first epoch of magmatism occurred in the Early Paleozoic (~500 to 405 Ma). These igneous rocks crop out roughly, but not well focused, on two sides of the ophiolite belt, termed "the North Orogenic belt" and "the South Orogenic belt" by *Xu et al.* [2013]. Rock assemblages of this magmatic epoch include the Bainaimiao arc volcanic-sedimentary sequence and granitoid plutons of varying size and composition (e.g., diorite, granodiorite, granite, and tonalite). The Bainaimiao volcanic-sedimentary sequence in the southern margin of the belt is well studied for its famous Cu-Mo-Au deposit [e.g., *Nie et al.*, 1994]. Volcanic rocks in this sequence mainly consist of foliated massive basalt and basaltic andesite interlayered with felsic rocks, indicating a bimodal compositional range. The basaltic rocks are calc-alkaline and exhibit typical CAB affinity [*Liu et al.*, 2014], and their formation ages have been determined to be ~465–440 Ma [*Miao et al.*, 2007; *Liu et al.*, 2014; *Li et al.*, 2015].

This cycle of magmatism is coincident with the contemporaneous magmatic activity in the whole Tianshan orogen, the western segment of the CAOB (510–420 Ma) in China [e.g., *Gao et al.*, 2009; *Pu et al.*, 2011]. Consequently, magmatic ages of both volcanic and plutonic rocks on the whole scale of the CAOB indicate that the first cycle of orogeny started at least at ~510 Ma and ended at ~405 Ma. This orogeny is an accretionary event by seafloor subduction without intensive continental collision and crustal shortening/thickening.

The second magmatic epoch lasted ~140 Myr from the beginning of the Carboniferous (~360 Ma) to the Early Triassic (~220 Ma). There is an approximately ~50 Myr interval between the two magmatic epochs. Rock types in this magmatic event include calc-alkaline, high-K calc-alkaline, and alkaline plutons (gabbro, diorite, granodiorite, and granite) [see *Tong et al.*, 2015] and the widely distributed Dashizhai volcanic formation (315–250 Ma). The rock assemblages and geochemistry suggest that this epoch of magmatism reflect an arc (mostly oceanic arc) environment in response to seafloor subduction (see below).

5.4. Carboniferous and Triassic Magmatism: Arc or Long-Lived Postcollisional Extension?

The second epoch of magmatism, including various plutonic and volcanic rocks, took place in a time span of ~140 Myr from 360 Ma to 220 Ma (Figure 13). Such a long-lived magmatic activity cannot be interpreted as postcollisional extension or intracontinental rifting but is consistent with long-lived subduction and arc/back-arc magmatism. In the northern NCC, magmatic activity occurred contemporaneously in the same

time period from 360 Ma to 210 Ma [e.g., *S.-H. Zhang et al*., 2007a, 2007b, 2010]. The alkaline magmatic belt of 250–210 Ma, together with adakitic rocks, suggests a back-arc extension caused by retreating of trench/subduction zone [e.g., *Niu*, 2014] of the New Paleo-Asian Ocean [*Wang et al*., 2015]. Their compositions vary with a trend of increasing K southward to the NCC continental margin with time [*Jahn et al*., 2009; *Zhang et al*., 2012]. This trend suggests magmatic compositions varying from oceanic arc, to continental margin to inner continent, similar to the present-day Japanese arc to continental China.

The Dashizai volcanic formation is widespread in the whole Eastern CAOB, from Mandulan, Solonker to the west, via Xilinhot, Linxi, to the northeast border of China (out of Figure 1). This volcanic complex is predominantly calc-alkaline with minor shoshonite and tholeiitic series in composition, with lithologies ranging from basalt, andesite, dacite, and rhyolite [e.g., *Shao*, 1991; *Lu et al*., 2002; *Zhang et al*., 2011; *Cao et al*., 2012; *Cheng et al*., 2013; *Li et al*., 2014; *Fan et al*., 2014], and clear geochemical signatures of island arc/active continental margins. A high percentage of magmatism is calc-alkaline, with rocks from basalt, andesite dacite to rhyolite, and no obvious bimodality.

Geochronological studies reveal that the ages of the Dashizhai Formation range from 315 Ma to 250 Ma [*Cao et al*., 2012; *Chen et al*., 2012; *Cheng et al*., 2013; *Li et al*., 2014; *Xu et al*., 2014; *Fan et al*., 2014], with the time interval much longer than the mantle plume magmatism in Tarim (290–270 Ma) [*Tian et al*., 2010] or the Siberian Trap (~250 Ma) [e.g., *Sun et al*., 2012].

5.5. Hard or Soft Continental Collision in the CAOB?

Continental collision follows seafloor subduction after an ocean plate is totally consumed, which can lead to finite extent of continental subduction, intensive crustal shortening/thickening, as well as high-grade (UHP, HP to MP, and HT) metamorphism and syncollisional and postcollisional magmatism [e.g., *O'Brien*, 2001; *Song et al*., 2006, 2014, 2015; *M. Wang et al*., 2014]. This orogenic procedure may be called "hard collision" in the Himalayan case [e.g., *van Hinsbergen et al*., 2012]. Hard collision and continental subduction between two convergent continental plates require two basic conditions: (1) prior oceanic plate subduction and (2) "passive margin" connected continental lithosphere [*Song et al*., 2014].

However, when an ocean lithosphere has bidirectional subduction zones along its two borders, the situation is different. In this case, there is no passive continental margin and thus no continental lithosphere can be dragged into subduction zones. Hence, soft collision between the two convergent continents would occur, similar to the case of Appalachian orogen in North America [e.g., *Draut and Clift*, 2001, 2013] with no large-scale continental shortening and thickening and no HP-UHP/HT metamorphic rocks can be exhumed. We term such orogeny as "Appalachian-type" or "CAOB-type" collision.

Beside the ~400 km wide distribution of ophiolite blocks, arc magmatism and accretionary complex with two epochs of 500–410 and 360–220 Ma described above, the following lines of evidence indicate that the CAOB is a type of the accretionary orogenic belt that had experienced soft collision between the convergent continents without crustal shortening and mountain building [*Windley et al*., 1990, 2007; *Xiao et al*., 2003, 2009a; *Kröner et al*., 2007, 2014].

1. According to the distribution of igneous rocks in the eastern segment of the CAOB, most researchers agree that the CAOB experienced bilateral subduction predominantly in its evolution history [e.g., *Xiao et al*., 2003, 2009a, 2013; *Windley et al*., 1990, 2007; *Miao et al*., 2007, 2008; *Chen et al*., 2009; *Xu et al*., 2013, 2014; *S.-H. Zhang et al*., 2014].
2. The thickness of the CAOB crust is ~40–45 km [*S. Zhang et al*., 2014], and no subsequent destruction of the crust has happened in the Mesozoic and Cenozoic. Therefore, the crust in the whole region of the Xing'an-Mongolia segment of the CAOB has not been greatly thickened during its orogenic history. No evidence for large overthrusting on the scale of the Himalayan or Alpine thrust sheets has been reported.
3. Most rocks in the belt have suffered from low-grade metamorphism, including blueschist [*Xu et al*., 2013; *J. Zhang et al*., 2015], greenschist, and lower amphibolite facies rocks. Although there are some high-grade metamorphic rocks ($T = 750–800°C$, $P = 4.7–5.5$ kbar) with anatexis veins in the Xinlinhot metamorphic belt (C. J. Wei et al., unpublished data, 2015), they are most likely associated with low-pressure metamorphism in an arc setting. No high-pressure ($P > 8$ kbar) granulite facies metamorphic rocks, which usually appear in most collisional orogenic belts like Himalaya, have been reported. This means no strong collisions between the two convergent continents.

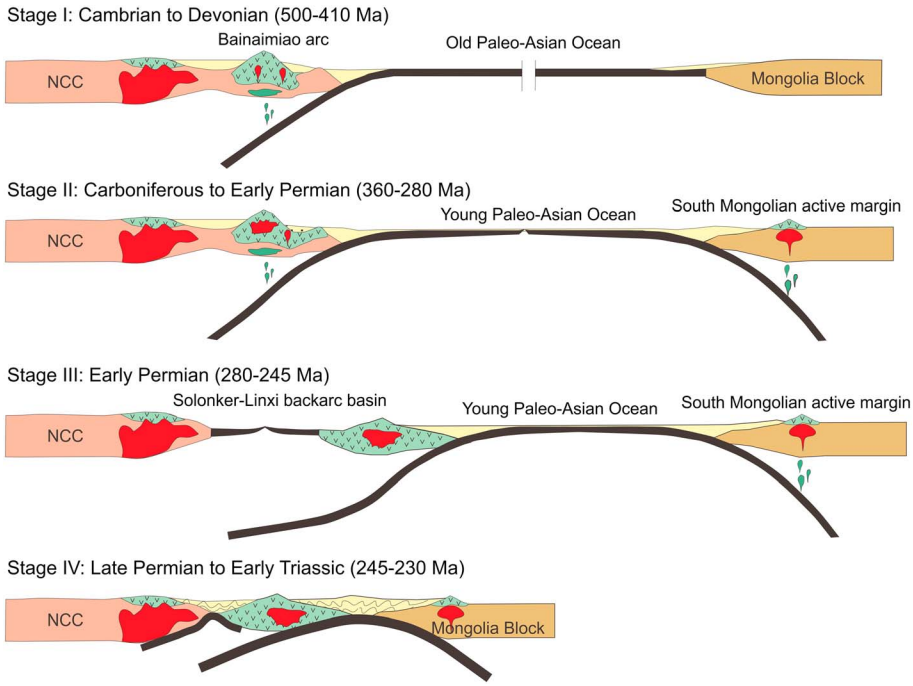

Figure 14. Schematic cartoons illustrating the tectonic evolution of the Xing'an-Inner Mongolia Accretionary Belt of the CAOB. Positions of the South Mongolian active margin are after *Badarch et al*. [2002] and *Xiao et al*. [2003].

4. Ultrahigh-pressure (UHP) metamorphism of continental crust, which means one continent subducted to mantle depths (>80 km) beneath another, has not been observed throughout the CAOB within the boarder of China.

5.6. Tectonic Evolution: Two Epochs of Seafloor Spreading and Two Cycles of Accretionary Events

The tectonic evolution of the CAOB has been hotly debated. *Windley et al*. [2007] and *Xiao et al*. [2009a] suggested a long-lived accretionary history from the Neoproterozic to Triassic. *Xu et al*. [2013, 2014, 2015] suggested that the Paleo-Asian Ocean closed and collision between the Mongolian block and the NCC occurred in the Devonian. Based on geochemical data of granitoids, *Jahn et al*. [2009] and *Han et al*. [2011] concluded that the Paleo-Asian Ocean has closed at ~310–300 Ma and a significant geodynamic change in CAOB occurred at ~300 Ma, which may be caused by delamination of the thickened lithospheric root and asthenospheric upwelling of postcollisional or rifting events.

According to formation ages of ophiolites and the nearly concurrent magmatic activity reported in this study, two cycles/epochs of oceans could exist in the Xing'an-Mongolia segment of the CAOB, of which we name them "the Old Paleo-Asian Ocean (OPAO)" and "the Young Paleo-Asian Ocean (YPAO)," respectively.

The OPAO might have developed from the Neoproterozoic [e.g., *Xiao et al*., 2003; *Windley et al*., 2007]. Magmatism and blueschist ages suggested that the subduction of the OPAO started at about 510–500 Ma [*Xu et al*., 2014, 2015] but stopped at ~410 Ma, with no hard collision and no postcollisional metamorphism/magmatism.

When the Young Paleo-Asian Ocean (YPAO) started is unknown. We do not know if it was a newly developed, independent ocean or if it evolved from the former OPAO. The 50 Myr gap without magmatic and metamorphic record suggests two separate cycles of oceanic events. The ophiolite (360–250 Ma) and coeval magmatic activity (360–220 Ma) suggest a long-lived interaction between seafloor subduction, island arc/continental arc, and back-arc basin and continuously accreted to both margins of the NCC in the south and the Mongolia block in the north. Subduction toward the Mongolia block in the north could be an Andean-type margin without back-arc extension, while southward subduction to the NCC would most likely develop into a western Pacific-type trench-arc-back-arc basin system at about 280 Ma, as supported by the Mandula ophiolite and Xingshuwa ophiloite.

On the basis of the foregoing discussion, the inferred tectonic evolution of the XIMAB of the CAOB from seafloor spreading, subduction, development of arc and back-arc system, and final closure of the Paleo-Asian Ocean is illustrated in Figure 14 in four major stages.

Stage I (*Cambrian to Devonian*, *the Early Paleozoic orogenic cycle of the OPAO*). Southward seafloor subduction initiated at ~ 500 Ma and formed the Bainaimiao arc volcanic sequence on the northern margin of the NCC and granitoids with ages of 500–410 Ma. However, we do not know if the OPAO was totally closed as emphasized by *Xu et al*. [2013, 2015] or remained inactive for ~ 50 Myr.

Stage II (*Carboniferous to Early Permian*, *the Late Paleozoic orogenic cycle of the YPAO*). Bilateral seafloor subduction (double divergent subduction) of the YPAO occurred at ~ 360 Ma, the beginning of the Carboniferous era, with intensive magmatic activity that widely spreads in the whole 400 km wide XIMAB of the CAOB and its both sides of the continental margin, including plutonic and volcanic rocks with ages from 360 Ma to 280 Ma.

Stage III (*Middle Permian to Early Triassic*, *the late stage of the YPAO*). Back-arc extension on the active margin of the NCC occurred at ~ 280 Ma, lasted to ~ 245 Ma, and formed the Solonker-Linxi SSZ-type ophiolite belt.

Stage IV (*Early to Middle Triassic*). The YPAO was finally closed, and soft collision between the NCC and the Mongolia Microcontinent occurred, which gave rise to the crustal extension that formed an alkaline magmatic belt along the northern margin of the NCC [e.g., *W. Zhang et al*., 2010] and the onset of the NCC lithosphere destruction [e.g., *Yang and Wu*, 2009; *Wang et al*., 2015].

Acknowledgments

Data supporting Figure 8 are available as in the supporting information Tables S1 and S2. Data supporting Figure 5 are available as in the supporting information Tables S3 and S4. All the data for this paper are available by contacting the corresponding author. This study was supported by the National Key Basic Research Program of China (2013CB429806) and the National Natural Science Foundation of China (grants 41372060, 41121062, and 41130314). We thank B. Xu, P. Zhao, Z.W. Luo, and Y.Y. Wang for their help in the field, X-H. Li and the SIMS group for their help in zircon age dating, and Z.B. Xiao and W.P. Zhu for Sr–Nd isotope analyses. We also thank the Editors and five anonymous reviewers for their constructive review comments.

References

Andersen, T. (2002), Correction of common lead in U-Pb analyses that do not report 204Pb, *Chem. Geol.*, *192*, 59–79.

Arai, S., and K. Matsukage (1996), Petrology of the gabbro-troctolite-peridotite complex from Hess Equatorial Pacific: Implications for mantle-melt interaction within the oceanic lithosphere, in *Proceedings of the Ocean Drilling Program*, *Sci. Results*, vol. 147, edited by C. Mevel et al., pp. 135–155, College Station, Tex.

Badarch, G., W. Dickson Cunningham, and B. F. Windley (2002), A new terrane subdivision for Mongolia: Implications for the Phanerozoic crustal growth of Central Asia, *J. Asian Earth Sci.*, *21*(1), 87–110.

Bao, Z. W., S. H. Chen, and Z. T. Zhang (1994), A study on REE and Sm-Nd isotopes of Hegenshan ophiolite, Inner Mongolia, *Geochemica*, *23*, 339–349.

Black, L. P., S. L. Kamo, C. M. Allen, J. N. Aleinikoff, D. W. Davis, R. J. Korsch, and C. Foudoulis (2003), TEMORA 1: A new zircon standard for Phanerozoic U–Pb geochronology, *Chem. Geol.*, *200*, 155–170.

Bureau of Geology and Mineral Resources of Inner Mongolia (BGMRIM) (1991), *Regional Geology of Nei Mongol (Inner Mongolia) Autonomous Region* [in Chinese with English summary], *Geol. Mem., Ser. 2*, vol. 25, 725 pp., Geol. Publ. House, Beijing.

Buslov, M. M., I. Y. Saphonova, T. Watanabe, O. T. Obut, Y. Fujiwara, K. Iwata, N. N. Semakov, Y. Sugai, L. V. Smirnova, and A. Y. Kazansky (2001), Evolution of the Paleo-Asian Ocean (Altai-Sayan Region, Central Asia) and collision of possible Gondwana-derived terranes with the southern marginal part of the Siberian continent, *Geosci. J.*, *5*, 203–224.

Cao, H.-H., W.-L. Xu, F.-P. Pei, P. Y. Guo, and F. Wang (2012), Permian tectonic evolution of the eastern section of the northern margin of the North China Plate: Constraints from zircon U–Pb geochronology and geochemistry of the volcanic rocks, *Acta Petrol. Sin.*, *28*, 2733–2750.

Cao, H.-H., W.-L. Xu, F.-P. Pei, Z.-W. Wang, F. Wang, and Z.-J. Wang (2013), Zircon U–Pb geochronology and petrogenesis of the Late Paleozoic–Early Mesozoic intrusive rocks in the eastern segment of the northern margin of the North China Block, *Lithos*, *170–171*, 191–207.

Chen, B., B.-m. Jahn, S. Wilde, and B. Xu (2000), Two contrasting Paleozoic magmatic belts in northern Inner Mongolia, China: Petrogenesis and tectonic implications, *Tectonophysics*, *328*(1–2), 157–182.

Chen, B., B. M. Jahn, and W. Tian (2009), Evolution of the Solonker suture zone: Constraints from zircon U–Pb ages, Hf isotopic ratios and whole-rock Nd–Sr isotope compositions of subduction- and collision-related magmas and forearc sediments, *J. Asian Earth Sci.*, *34*, 245–257.

Chen, C., Z. C. Zhang, Z. J. Guo, J. F. Li, Z. S. Feng, and W. H. Tang (2012), Geochronology, geochemistry, and its geological significance of the Permian Mandula mafic rocks in Damaoqi, Inner Mongolia, *Sci. China Earth Sci.*, *55*, 39–52.

Cheng, T. Q., W. J. Yang, and D. H. Wang (2013), Zircon U-Pb age of the spilite-keratophyre sequence of the Dashizhai formation in the Maodeng of Xilinhaote, Inner Mongolia and its geological significance, *Geoscience*, *27*, 525–536.

Chu, H., J. Zhang, C. Wei, H. Wang, and Y. Ren (2013), A new interpretation of the tectonic setting and age of meta-basic volcanics in the Ondor Sum Group, Inner Mongolia, *Chin. Sci. Bull.*, *58*, 3580–3587.

Cocks, L. R. M., and T. H. Torsvik (2007), Siberia, the wandering northern terrane, and its changing geography through the Palaeozoic, *Earth Sci. Rev.*, *82*, 29–74.

Coleman, R. G. (1977), *Ophiolites*, pp. 220, Springer, New York.

Dewey, J. F., and J. M. Bird (1971), The origin and emplacement of the ophiolite suite: Appalachian ophiolites in Newfoundland, *J. Geophys. Res.*, *76*, 3179–3206, doi:10.1029/JB076i014p03179.

Dick, H. J. B., and T. Bullen (1984), Chromian spinel as a petrogenetic indicator in abyssal and alpine-type peridotites and spatially associated lavas, *Contrib. Mineral. Petrol.*, *86*, 54–76.

Dilek, Y. (2003), Ophiolite concept and its evolution, *Geol. Soc. Am. Spec. Pap.*, *373*, 1–16.

Dilek, Y., and H. Furnes (2011), Ophiolite genesis and global tectonics: Geochemical and tectonic fingerprinting of ancient oceanic lithosphere, *Geol. Soc. Am. Bull.*, *123*, 387–411.

Dilek, Y., H. Furnes, and M. Shallo (2007), Suprasubduction zone ophiolite formation along the periphery of Mesozoic Gondwana, *Gondwana Res.*, *11*, 453–475.

Draut, A. E., and P. D. Clift (2001), Geochemical evolution of arc magmatism during arc-continent collision, South Mayo, Ireland, *Geology*, *29*, 543–546.

Draut, A. E., and P. D. Clift (2013), Differential preservation in the geologic record of intraoceanic arc sedimentary and tectonic processes, *Earth Sci. Rev.*, *116*, 57–84.

Drouin, M., B. Ildefonse, and M. Godard (2010), A microstructural imprint of melt impregnation in slow spreading lithosphere: Olivine-rich troctolites from the Atlantis Massif, Mid-Atlantic Ridge, 30°N, IODP Hole U1309D, *Geochem. Geophys. Geosyst.*, *11*, Q06003, doi:10.1029/2009GC002995.

Eizenhöfer, P. R., G. Zhao, J. Zhang, and M. Sun (2014), Final closure of the Paleo-Asian Ocean along the Solonker Suture Zone: Constraints from geochronological and geochemical data of Permian volcanic and sedimentary rocks, *Tectonics*, *33*, 441–463, doi:10.1002/2013TC003357.

Fan, H. Y., M. C. Li, Q. Zhang, M. Huang, X. F. Zhang, and J. J. Li (2014), Age and geochemical characteristics of the Dashizai Formation volcanic rocks in Xi Ujimqin Banner, Inner Mongolia, *Geol. Bull. China*, *33*, 1284–1292.

Gaetani, G. A., T. L. Grove, and W. B. Bryan (1993), The influence of water on the petrogenesis of subduction-related igneous rocks, *Nature*, *365*, 332–334.

Gao, J., L. Long, R. Klemd, Q. Qian, D. Liu, X. Xiong, W. Su, W. Liu, Y. Wang, and F. Yang (2009), Tectonic evolution of the South Tianshan orogen and adjacent regions, NW China: Geochemical and age constraints of granitoid rocks, *Int. J. Earth Sci. (Geol. Rundsch.)*, *98*, 1221–1238.

Gillis, K. M., et al. (2014), Primitive layered gabbros from fast-spreading lower oceanic crust, *Nature*, *505*, 204–207.

Han, B.-F., G.-Q. He, X.-C. Wang, and Z.-J. Guo (2011), Late Carboniferous collision between the Tarim and Kazakhstan–Yili terranes in the western segment of the South Tian Shan Orogen, Central Asia, and implications for the Northern Xinjiang, western China, *Earth Sci. Rev.*, *109*, 74–93.

He, G. Q., and J. A. Shao (1983), Determination of Early Paleozoic ophiolites in southeastern Nei Mongol and their geotectonic significance, in *Contributions for the Project of Plate Tectonics in Northern China*, vol. 1, edited by K. D. Tang, pp. 243–250, Geological Publishing House, Beijing.

Hsü, K. J., Q. Wang, J. Li, and J. Hao (1991), Geologic evolution of the Neimonides: A working hypothesis, *Eclogae Geol. Helv.*, *84*, 1–31.

Hu, C., W. Li, C. Xu, R. Zhong, and F. Zhu (2015), Geochemistry and zircon U–Pb–Hf isotopes of the granitoids of Baolidao and Halatu plutons in Sonidzuoqi area, Inner Mongolia: Implications for petrogenesis and geodynamic setting, *J. Asian Earth Sci.*, *97*, 294–306.

Jahn, B. M. (2004), The Central Asian Orogenic Belt and growth of the continental crust in the Phanerozoic, in *Aspects of the Tectonic Evolution of China*, edited by J. Malpas et al., *Geol. Soc. London Spec. Publ.*, *226*, pp. 73–100.

Jahn, B. M., F. Y. Wu, and B. Chen (2000), Massive granitoid generation in Central Asia: Nd isotope evidence and implication for continental growth in the Phanerozoic, *Episodes*, *23*, 82–92.

Jahn, B. M., B. A. Litvinovsky, A. N. Zanvilevich, and M. Reichow (2009), Peralkaline granitoid magmatism in the Mongolian–Transbaikalian Belt: Evolution, petrogenesis and tectonic significance, *Lithos*, *113*, 521–539.

Jian, P., Y. R. Shi, F. Q. Zhang, L. C. Miao, L. Q. Zhang, and A. Kröner (2007), Geological excursion to Inner Mongolia, China, to study the accretionary evolution of the southern margin of the Central Asian Orogenic Belt, edited by D. Y. Liu et al., Abstract and Excursion Guidebook, Third International Workshop and Field Excursion for IGCP Project, 480, pp. 49–72.

Jian, P., et al. (2008), Time scale of an early to mid-Paleozoic orogenic cycle of the long-lived Central Asian Orogenic Belt, Inner Mongolia of China: Implications for continental growth, *Lithos*, *101*, 233–259.

Jian, P., D. Liu, A. Kröner, B. F. Windley, Y. Shi, W. Zhang, F. Zhang, L. Miao, L. Zhang, and D. Tomurhuu (2010), Evolution of a Permian intraoceanic arc–trench system in the Solonker suture zone, Central Asian Orogenic Belt, China and Mongolia, *Lithos*, *118*, 169–190.

Jian, P., A. Kröner, B. F. Windley, Y. Shi, W. Zhang, L. Zhang, and W. Yang (2012), Carboniferous and Cretaceous mafic–ultramafic massifs in Inner Mongolia (China): A SHRIMP zircon and geochemical study of the previously presumed integral "Hegenshan ophiolite", *Lithos*, *142–143*, 48–66.

Kamenetsky, V. S., A. J. Crawford, and A. S. Meffre (2001), Factors controlling chemistry of magmatic spinel: An empirical study of associated olivine, Cr-spinel and melt inclusions from primitive rocks, *J. Petrol.*, *42*, 655–671.

Kröner, A., B. F. Windley, G. Badarch, O. Tomurtogoo, E. Hegner, B. M. Jahn, S. Gruschka, E. V. Khain, A. Demoux, and M. T. D. Wingate (2007), Accretionary growth and crust formation in the Central Asian Orogenic Belt and comparison with the Arabian-Nubian shield, *Geol. Soc. Am. Mem.*, *200*, 181–209.

Kröner, A., et al. (2014), Reassessment of continental growth during the accretionary history of the Central Asian Orogenic Belt, *Gondwana Res.*, *25*(1), 103–125, doi:10.1016/j.gr.2012.12.023.

Li, J. Y. (1987), Essential characteristics of Early Paleozoic ophiolites to North of Xar Moron River, eastern Nei Mongol and their plate tectonic significance, in *Shenyang Institute of Geology and Mineral Resource*, *Contrib. Proj. Plate Tecton. North. China*, vol. 2, edited by K. D. Tang, pp. 136–150, Geological Publishing House.

Li, J. Y. (2006), Permian geodynamic setting of Northeast China and adjacent regions: Closure of the Paleo-Asian Ocean and subduction of the Paleo-Pacific Plate, *J. Asian Earth Sci.*, *26*, 207–224.

Li, J. Y., L. M. Gao, G. H. Sun, Y. P. Li, and Y. B. Wang (2007), Shuangjingzi middle Triassic syncollisonal crust-derived granite in the eastern Inner Mongolia and its constraint on the timing of collision between Siberian and Sino–Korean paleo-plates, *Acta Petrol. Sin.*, *23*, 565–582.

Li, K., Z. C. Zhang, J. F. Feng, W. H. Tang, and Z. W. Luo (2014), Zircon SHRIMP U-Pb dating and its geological significance of the Late Carboniferous to Early Permian volcanic rocks in Bayanwula area, the central of Inner Mongolia, *Acta Petrol. Sin.*, *30*, 2041–2054.

Li, Q.-L., X.-H. Li, Y. Liu, G.-Q. Tang, J.-H. Yang, and W.-G. Zhu (2010), Precise U-Pb and Pb-Pb dating of Phanerozoic baddeleyite by SIMS with oxygen flooding technique, *J. Anal. At. Spectrom.*, *25*, 1107–1113.

Li, W., C. Hu, R. Zhong, and F. Zhu (2015), U–Pb, 39Ar/40Ar geochronology of the metamorphosed volcanic rocks of the Bainaimiao Group in central Inner Mongolia and its implications for ore genesis and geodynamic setting, *J. Asian Earth Sci.*, *97*, 251–259.

Li, X., G. Tang, B. Gong, Y. Yang, K. Hou, Z. Hu, Q. Li, Y. Liu, and W. Li (2013), Qinghu zircon: A working reference for microbeam analysis of U-Pb age and Hf and O isotopes, *Chin. Sci. Bull.*, *58*, 4647–4654.

Li, X.-H., Y. Liu, Q.-L. Li, C.-H. Guo, and K. R. Chamberlain (2009), Precise determination of Phanerozoic zircon Pb/Pb age by multicollector SIMS without external standardization, *Geochem. Geophys. Geosyst.*, *10*, Q04010, doi:10.1029/2009GC002400.

Li, Y. J., J. F. Wang, H. Y. Li, P. P. Dong, Y. C. Liu, D. W. Liu, and H. Bai (2012), Recognition of Diyanmiao ophiolite in Xi U jimqin Banner, Inner Mongolia, *Acta Petrol. Sin.*, *28*, 1282–1290.

Liang, R. X. (1994), The features of ophiolites in the central sector of Inner Mongolia and its geological significance, *Reg. Geol. China*, *1*, 37–45.

Lister, G., and M. Forster (2009), Tectonic mode switches and the nature of orogenesis, *Lithos*, *113*, 274–291.

Liu, C. F., W. C. Liu, H. P. Wang, G. Z. Zhou, H. F. Zh, and Y. J. Tang (2014), Geochronology and geochemistry of the Bainianmiao metavolcanic rocks in the Northern Margin of North China Craton, *Acta Geol. Sin.*, *88*, 1273–1287.

Liu, D. Y., P. Jian, and Q. Zhang (2003), SHRIMP dating of adakites in the Tulingkai ophiolite, Inner Mongolia: Evidence for the Early Paleozoic subduction, *Acta Geol. Sin.*, *77*, 317–327.

Liu, J., J. Li, X. Chi, J. Qu, Z. Hu, S. Fang, and Z. Zhang (2013), A late-Carboniferous to early early-Permian subduction–accretion complex in Daqing pasture, southeastern Inner Mongolia: Evidence of northward subduction beneath the Siberian paleoplate southern margin, *Lithos*, *177*, 285–296.

Long, X., C. Yuan, M. Sun, I. Safonova, W. Xiao, and Y. Wang (2012), Geochemistry and U–Pb detrital zircon dating of Paleozoic graywackes in East Junggar, NW China: Insights into subduction–accretion processes in the southern Central Asian Orogenic Belt, *Gondwana Res.*, *21*, 637–653.

Lu, Z. C., G. Z. Duan, and L. B. Hao (2002), The petrological and geochemical characteristics and petrogenesis significance of spilite from lower Permian Dashizai Group in middle section of Da Hinggan Mountains, *Acta Petrol. Sin.*, *18*, 212–222.

Ludwig, K. R. (2003), *User's Manual for Isoplot 3.00: A Geochronological Toolkit for Microsoft Excel*, *Spec. Publ.*, vol. 4, Berkeley Geochronology Center, Berkeley, Calif.

Meschede, M. (1986), A method of discriminating between different types of mid-ocean ridge basalts and continental tholeiites with the Nb-Zr-Y diagram, *Chem. Geol.*, *56*, 207–218.

Miao, L., F. Zhang, W.-M. Fan, and D. Liu (2007), Phanerozoic evolution of the Inner Mongolia–Daxinganling orogenic belt in North China: Constraints from geochronology of ophiolites and associated formations, *Geol. Soc. London, Spec. Publ.*, *280*, 223–237.

Miao, L., W. Fan, D. Liu, F. Zhang, Y. Shi, and F. Guo (2008), Geochronology and geochemistry of the Hegenshan ophiolitic complex: Implications for late-stage tectonic evolution of the Inner Mongolia-Daxinganling Orogenic Belt, China, *J. Asian Earth Sci.*, *32*, 348–370.

Miyashiro, A. (1975), Classification, characteristics, and origin of ophiolites, *J. Geol.*, *83*, 249–281.

Nie, F. J., R. F. Pei, L. S. Wu, and A. Bjørlykke (1994), Nd, Sr and Pb isotopic study of copper (gold) and gold deposits in Bainaimiao area, Inner Mongolia, *Miner. Deposits*, *13*, 331–344.

Niu, Y., and R. Batiza (1997), Trace element evidence from seamounts for recycled oceanic crust in the Eastern Pacific mantle, *Earth Planet. Sci. Lett.*, *148*, 471–483.

Niu, Y., and R. Hekinian (1997), Spreading-rate dependence of the extent of mantle melting beneath ocean ridges, *Nature*, *385*(6614), 326–329.

Niu, Y., and M. J. O'Hara (2009), MORB mantle hosts the missing Eu (Sr, Nb, Ta and Ti) in the continental crust: New perspectives on crustal growth, crust–mantle differentiation and chemical structure of oceanic upper mantle, *Lithos*, *112*, 1–17.

Niu, Y., D. Bideau, R. Hékinian, and R. Batiza (2001), Mantle compositional control on the extent of mantle melting, crust production, gravity anomaly, ridge morphology, and ridge segmentation: A case study at the Mid-Atlantic Ridge 33–35°N, *Earth Planet. Sci. Lett.*, *186*, 383–399.

Niu, Y., M. Regelous, I. J. Wendt, R. Batiza, and M. J. O'Hara (2002), Geochemistry of near-EPR seamounts: Importance of source vs. process and the origin of enriched mantle component, *Earth Planet. Sci. Lett.*, *199*, 327–345.

Niu, Y. L. (2014), Geological understanding of plate tectonics: Basic concepts, illustrations, examples and new perspectives, *Global Tecton. Metallog.*, *10*, 1–24.

Niu, Y. L., K. D. Collerson, R. Batiza, J. I. Wendt, and M. Regelous (1999), The origin of E-Type MORB at ridges far from mantle plumes: The East Pacific Rise at 11°20′N, *J. Geophys. Res.*, *104*, 7067–7087, doi:10.1029/1998JB900037.

Nozaka, T., and Y. Liu (2002), Petrology of the Hegenshan ophiolite and its implication for the tectonic evolution of northern China, *Earth Planet. Sci. Lett.*, *202*(1), 89–104.

O'Brien, P. J. (2001), Subduction followed by collision: Alpine and Himalayan examples, *Phys. Earth Planet. Inter.*, *127*, 277–291.

Pearce, J. A. (2003), Supra-subduction zone ophiolites: The search for modern analogues, *Geol. Soc. Am. Spec. Pap.*, *373*, 269–293.

Pearce, J. A. (2008), Geochemical fingerprinting of oceanic basalts with applications to ophiolite classification and the search for Archean oceanic crust, *Lithos*, *100*, 14–48.

Pearce, J. A., and P. T. Robinson (2010), The Troodos ophiolitic complex probably formed in a subduction initiation, slab edge setting, *Gondwana Res.*, *18*, 60–81.

Pearce, J. A., S. J. Lippard, and S. Roberts (1984), Characteristics and tectonic significance of supra-subduction zone ophiolites, *Spec. Publ. Geol. Soc. London*, *16*(1), 77–94.

Pearce, J. A., P. F. Barker, S. J. Edwards, I. J. Parkinson, and P. T. Leat (2000), Geochemistry and tectonic significance of peridotites from the South Sandwich arc–basin system, South Atlantic, *Contrib. Mineral. Petrol.*, *139*, 36–53.

Pu, X. F., S. G. Song, L. F. Zhang, and C. J. Wei (2011), Silurian arc volcanic slices and their tectonic implications in the southwestern Tianshan UHPM belt, NW China, *Acta Petrol. Sin.*, *27*, 1675–1687.

Regelous, M., Y. Niu, J. I. Wendt, R. Batiza, A. Greig, and K. D. Collerson (1999), Variations in the geochemistry of magmatism on the East Pacific Rise at 10°30′N since 800 ka, *Earth Planet. Sci. Lett.*, *168*, 45–63.

Robinson, P. T., M.-f. Zhou, X.-F. Hu, P. Reynolds, B. Wenji, and J. Yang (1999), Geochemical constraints on the origin of the Hegenshan Ophiolite, Inner Mongolia, China, *J. Asian Earth Sci.*, *17*(4), 423–442.

Shao, J. A. (1991), *Crust Evolution in the Middle Part of the Northern Margin of Sino-Korean Plate*, pp. 1–136, Peking Univ. Publishing House, Beijing.

Sláma, J., et al. (2008), Plešovice zircon—A new natural reference material for U–Pb and Hf isotopic microanalysis, *Chem. Geol.*, *249*, 1–35.

Song, S. G., L. F. Zhang, Y. L. Niu, L. Su, B. Song, and D. Y. Liu (2006), Evolution from oceanic subduction to continental collision: A case study from the northern Tibetan Plateau based on geochemical and geochronological data, *J. Petrol.*, *47*, 435–455.

Song, S. G., Y. L. Niu, C. J. Wei, J. Q. Ji, and L. Su (2010), Metamorphism, anatexis, zircon ages and tectonic evolution of the Gongshan block in the northern Indochina continent—An eastern extension of the Lhasa Block, *Lithos*, *120*, 327–346.

Song, S. G., Y. L. Niu, L. Su, and X. H. Xia (2013), Tectonics of the North Qilian orogen, NW China, *Gondwana Res.*, *23*, 1378–1401.

Song, S. G., Y. L. Niu, L. Su, C. Zhang, and L. F. Zhang (2014), Continental orogenesis from ocean subduction, continent collision/subduction, to orogen collapse, and orogen recycling: The example of the North Qaidam UHPM belt, NW China, *Earth Sci. Rev.*, *129*, 59–84.

Song, S. G., M. J. Wang, C. Wang, and Y. L. Niu (2015), Magmatism during continental collision, subduction, exhumation and mountain collapse in collisional orogenic belts and continental net growth: A perspective, *Sci. China Earth Sci.*, *58*, 1284–1304.

Stacey, J. S., and J. D. Kramers (1975), Approximation of terrestrial lead isotope evolution by a two-stage model, *Earth Planet. Sci. Lett.*, *26*, 207–221.

Sun, S.-S., and W. F. McDonough (1989), Chemical and isotopic systematics of ocean basalt: Implications for mantle composition and processes, in *Magmatism in Ocean Basins*, edited by A. D. Saunders and M. J. Norry, *Geol. Soc. London Spec. Publ.*, 42, pp. 313–345.

Sun, Y., M. M. Joachimski, P. B. Wignall, C. Yan, Y. Chen, H. Jiang, L. Wang, and X. Lai (2012), Lethally hot temperatures during the Early Triassic greenhouse, *Science*, *338*, 366–370.

Tamura, A., and S. Arai (2006), Harzburgite–dunite–orthopyroxenite suite as a record of supra-subduction zone setting for the Oman ophiolite mantle, *Lithos*, *90*(1–2), 43–56.

Tian, W., I. Campbell, C. Allen, P. Guan, W. Pan, M. Chen, H. Yu, and W. Zhu (2010), The Tarim picrite–basalt–rhyolite suite, a Permian flood basalt from northwest China with contrasting rhyolites produced by fractional crystallization and anatexis, *Contrib. Mineral. Petrol.*, *160*, 407–425.

Tong, Y., B.-m. Jahn, T. Wang, D.-w. Hong, E. I. Smith, M. Sun, J.-f. Gao, Q.-d. Yang, and W. Huang (2015), Permian alkaline granites in the Erenhot–Hegenshan belt, northern Inner Mongolia, China: Model of generation, time of emplacement and regional tectonic significance, *J. Asian Earth Sci.*, *97*, 320–336.

van Hinsbergen, D. J. J., P. C. Lippert, G. Dupont-Nivet, N. McQuarrie, P. V. Doubrovine, W. Spakman, and T. H. Torsvik (2012), Greater India Basin hypothesis and a two-stage Cenozoic collision between India and Asia, *Proc. Natl. Acad. Sci. U.S.A.*, *109*, 7659–7664.

Wang, C., S. G. Song, Y. L. Niu, and L. Su (2015), Late Triassic adakitic plutons within the Archean terrane of the North China Craton: Melting of the ancient lower crust at the onset of the lithospheric destruction, *Lithos*, *212–215*, 353–367.
Wang, M., S. Song, Y. Niu, and L. Su (2014), Post-collisional magmatism: Consequences of UHPM terrane exhumation and orogen collapse, N. Qaidam UHPM belt, NW China, *Lithos*, *210–211*, 181–198.
Wang, Q., and X. Liu (1986), Paleoplate tectonics between Cathaysia and Angaraland in Inner Mongolia of China, *Tectonics*, *5*, 1073–1088, doi:10.1029/TC005i007p01073.
Wang, Y. J., and Z. Y. Pan (1997), Discovery of Permian radiolarians in ophiolite belt on northern side of Xar Moron River, Nei Monggol and its geological significance, *Acta Palaeontol. Sin.*, *36*, 58–69.
Wang, Y. Y., B. Xu, S. D. Cheng, W. Liao, J. Shao, and Y. Wang (2014), Zircon U-Pb dating of the mafic lava from Wudaoshimen, Hexigten, Inner Mongolia and its geological significance, *Acta Petrol. Sin.*, *30*, 2055–2062.
White, W. M., A. W. Hofmann, and H. Puchelt (1987), Isotope geochemistry of Pacific Mid-Ocean Ridge Basalt, *J. Geophys. Res.*, *92*(B6), 4881–4893, doi:10.1029/JB092iB06p04881.
Wiedenbeck, M., P. AllÉ, F. Corfu, W. L. Griffin, M. Meier, F. Oberli, A. V. Quadt, J. C. Roddick, and W. Spiegel (1995), Three natural zircon standards for U-Th-Pb, Lu-Hf, trace element and REE analyses, *Geostand. Newsl.*, *19*(1), 1–23.
Winchester, J. A., and P. A. Floyd (1977), Geochemical discrimination of different magma series and their differentiation products using immobile elements, *Chem. Geol.*, *20*, 325–343.
Windley, B. F., M. B. Allen, C. Zhang, Z.-Y. Zhao, and G.-R. Wang (1990), Paleozoic accretion and Cenozoic redeformation of the Chinese Tien Shan Range, central Asia, *Geology*, *18*(2), 128–131.
Windley, B. F., D. Alexeiev, W. Xiao, A. Kröner, and G. Badarch (2007), Tectonic models for accretion of the Central Asian Orogenic Belt, *J. Geol. Soc.*, *164*(1), 31–47.
Wood, D. A. (1980), The application of a Th-Hf-Ta diagram to problems of tectonomagmatic classification and to establishing the nature of crustal contamination of basaltic lavas of the British Tertiary Volcanic Province, *Earth Planet. Sci. Lett.*, *50*(1), 11–30.
Xia, X. H., S. G. Song, and Y. L. Niu (2012), Tholeiite-Boninite terrane in the North Qilian suture zone: Implications for subduction initiation and back-arc basin development, *Chem. Geol.*, *328*, 259–277.
Xiao, W. J., B. F. Windley, J. Hao, and M. Zhai (2003), Accretion leading to collision and the Permian Solonker suture, Inner Mongolia, China: Termination of the Central Asian Orogenic Belt, *Tectonics*, *22*(6), 1069, doi:10.1029/2002TC001484.
Xiao, W. J., F. Pirajno, and R. Seltmann (2008), Geodynamics and metallogeny of the Altaid orogen, *J. Asian Earth Sci.*, *32*, 77–81.
Xiao, W. J., B. F. Windley, B. C. Huang, C. M. Han, C. Yuan, H. L. Chen, M. Sun, S. Sun, and J. L. Li (2009a), End-Permian to mid-Triassic termination of the accretionary processes of the southern Altaids: Implications for the geodynamic evolution, Phanerozoic continental growth, and metallogeny of Central Asia, *Int. J. Earth Sci. (Geol. Rundsch.)*, *98*(6), 1189–1217.
Xiao, W. J., et al. (2009b), Paleozoic multiple subduction-accretion processes of the southern Altaids, *Am. J. Sci.*, *309*, 221–270.
Xiao, W., B. F. Windley, M. B. Allen, and C. Han (2013), Paleozoic multiple accretionary and collisional tectonics of the Chinese Tianshan orogenic collage, *Gondwana Res.*, *23*(4), 1316–1341.
Xu, B., J. Charvet, Y. Chen, P. Zhao, and G. Shi (2013), Middle Paleozoic convergent orogenic belts in western Inner Mongolia (China): Framework, kinematics, geochronology and implications for tectonic evolution of the Central Asian Orogenic Belt, *Gondwana Res.*, *23*(4), 1342–1364.
Xu, B., P. Zhao, Q. Z. Bao, Y. H. Zhou, Y. Y. Wang, and Z. W. Luo (2014), Preliminary study on the pre-Mesozoic tectonic unit division of the Xing-Meng Orogenic Belt (XMOB), *Acta Petrol. Sin.*, *30*, 1841–1857.
Xu, B., P. Zhao, Y. Wang, W. Liao, Z. Luo, Q. Bao, and Y. Zhou (2015), The pre-Devonian tectonic framework of Xing'an–Mongolia orogenic belt (XMOB) in north China, *J. Asian Earth Sci.*, *97*, 183–196.
Yang, J. H., and F. Y. Wu (2009), Triassic magmatism and its relation to decratonization in the eastern North China Craton, *Sci. China Earth Sci.*, *52*, 1319–1330.
Zhang, C., and T. R. Wu (1998), Sm-Nd, Rb-Sr isotopic isochron of metamorphic volcanic rocks of Ondor Sum Group, Inner Mongolia, *Chin. J. Geol.*, *33*, 25–30.
Zhang, J., C. Wei, and H. Chu (2015), Blueschist metamorphism and its tectonic implication of Late Paleozoic–Early Mesozoic metabasites in the mélange zones, central Inner Mongolia, China, *J. Asian Earth Sci.*, *97*, 352–364.
Zhang, S., et al. (2014), Crustal structures revealed from a deep seismic reflection profile across the Solonker suture zone of the Central Asian Orogenic Belt, northern China: An integrated interpretation, *Tectonophysics*, *612–613*, 26–39.
Zhang, S.-H., Y. Zhao, B. Song, and Y.-H. Yang (2007a), Zircon SHRIMP U–Pb and in-situ Lu–Hf isotope analyses of a tuff from Western Beijing: Evidence for missing Late Paleozoic arc volcano eruptions at the northern margin of the North China block, *Gondwana Res.*, *12*, 157–165.
Zhang, S.-H., Y. Zhao, B. Song, Z.-Y. Yang, J.-M. Hu, and A. H. Wu (2007b), Carboniferous granitic plutons from the northern margin of the North China block: Implications for a late Palaeozoic active continental margin, *J. Geol. Soc.*, *164*, 451–463.
Zhang, S.-H., Y. Zhao, J.-M. Liu, B. Song, J. Liu, and M. Wu (2010), Geochronology, geochemistry and tectonic setting of the Late Paleozoic-Early Mesozoic magmatism in the northern margin of the North China Block: A preliminary review, *Acta Petrol. Mineral.*, *29*, 824–842.
Zhang, S.-H., Y. Zhao, H. Ye, K.-J. Hou, and C.-F. Li (2012), Early Mesozoic alkaline complexes in the northern North China Craton: Implications for cratonic lithospheric destruction, *Lithos*, *155*, 1–18.
Zhang, S.-H., Y. Zhao, G. A. Davis, H. Ye, and F. Wu (2014), Temporal and spatial variations of Mesozoic magmatism and deformation in the North China Craton: Implications for lithospheric thinning and decratonization, *Earth Sci. Rev.*, *131*, 49–87.
Zhang, W., P. Jian, D. Y. Liu, and K. J. Hou (2010), Geochemistry, Geochronology and Hf isotopic compositions of Triassic granodiorite-diorite and shoshonite from the Damaoqi area, central Inner Mongolia, China, *Geol. Bull. China*, *29*, 821–832.
Zhang, X., S. A. Wilde, H. Zhang, and M. Zhai (2011), Early Permian high-K calc-alkaline volcanic rocks from NW Inner Mongolia, North China: Geochemistry, origin and tectonic implications, *J. Geol. Soc.*, *168*, 525–543.
Zhang, Z., K. Li, J. Li, W. Tang, Y. Chen, and Z. Luo (2015), Geochronology and geochemistry of the Eastern Erenhot ophiolitic complex: Implications for the tectonic evolution of the Inner Mongolia–Daxinganling Orogenic Belt, *J. Asian Earth Sci.*, *97*, 279–293.